Measurement and analysis of high altitude wind profiles over the sea in a coastal zone using a scanning doppler LiDAR: Application to wind energy

Alexandra Visich, Boris Conan

Measurement and analysis of high altitude wind profiles over the sea in a coastal zone using a scanning doppler LiDAR: Application to wind energy

Aleksandra Visich [1,*] and Boris Conan [2,*]

[1]UiT The Arctic University of Norway, Postboks 385, 8505 Narvik, Norway
[2]Nantes Université, Centrale Nantes, CNRS, LHEEA, UMR 6598, F-44321 Nantes, France
[*]These authors contributed equally to this work.

Correspondence: Boris Conan (boris.conan@ec-nantes.fr)

Abstract. The lack of observations at heights relevant to the wind energy industry constitutes a major challenge for the development of the next generation of offshore wind turbines (over 10 MW), which are expected to operate within the first few tens kilometres from the coast with turbine tips extending more than 250 m. Observations within the coastal zone, which proves to be complex by its very nature given that the site of sea breezes, low-level jets and land/sea transition are keys to both understanding the marine atmospheric boundary layer processes interacting with the turbine and parameterizing the wind profile well above the surface layer. These needs introduce difficulties associated with measuring wind properties in the region 150-500 m above the sea surface. This paper uses the virtual mast method to reconstruct the 10-min averaged wind profile 1.5 km offshore using a scanning Doppler LiDAR (Light Detection And Ranging) installed on the coastline. A novel method is proposed herein to increase the vertical resolution to 27 levels, from the sea surface to 500 m above sea level. Being mainly based on the homogeneity hypothesis, this method's sensitivity to wind direction is evaluated, while results are compared with reanalysis data at several heights. This method is then implemented as part of a 7-month test campaign on the northeastern Atlantic coast, yielding a dataset of wind profile measurements. An analysis of this dataset shows a 15.4% proportion of low-level jets, mainly originating from land at night, with a core well inside the rotor area of > 10 MW wind turbines. The power production is subsequently analysed for 10 MW, 15 MW and 22 MW wind turbines. Wind shear events above the design values are observed in 30% of all profiles, accounting for more than a third of the total power production. High shear events are found to be more probable during low-level jets (56% of the time), compared to no low-level jet events (26%). A description of low-level jets and high-shear events is thus key since these are situations where the wind profile differs from the standard values used for wind turbine design and may affect both the load and fatigue predictions.

1 Introduction

In Europe, between 2020 and 2022, newly connected offshore wind energy capacity accounted for roughly 2.8 GW per year, yielding a total connected capacity of 30.3 GW. This growth is expected to continue, through 2030, to reach a connected capacity of 135 GW (Ramirez, 2022). Over the last three years, newly installed offshore wind farms (whether fixed or floating) are located, for the most part, within the first 10-50 kilometres from the coast (Díaz and Soares, 2020), at an average distance from the coast of 44 km in 2020, 26 km in 2021, and 43 km in 2022 (Ramirez, 2022). From a meteorological standpoint, see (Rogers, 1995), the effects of the sea/land transition are still visible 100 km offshore. Hence, even with the advent of floating offshore turbines, which tend to increase the average distance to shore, most of these installations can be considered coastal rather than offshore. In 2022, 79% of the total offshore capacity was installed in the North Sea, 10% in the Irish Sea, and 9% in the Baltic Sea. Despite the considerable potential offered by the European Atlantic coast, as analysed by its levelized cost of energy by Martinez and Iglesias (2022), the connection to the grid in 2022 of the first French offshore wind farm at Saint-Nazaire also represented the first significant commercial wind farm along the entire European Atlantic coast, with 80 turbines installed 12 km from the coast.

Growing interest in the near offshore resource has led to more studies aimed at describing the physics of the marine atmospheric boundary layer (MABL) near the coast. This region, heterogeneous by its nature, combines onshore and offshore complexitiesk, i.e.: orographic change (coastline), roughness change, variation of the sea-surface temperature, strong contrast between ocean and land heat capacity, and enhanced dynamic interaction between the water surface and the lower part of the MABL by means of waves, coastal bathymetry, local currents and tidal dynamics (Rogers, 1995; Garratt, 1994). These multi-scale interactions produce complex local atmospheric flow phenomena (Archer et al., 2014), such as the wave boundary layer, boundary-layer transitions, coastal low-level jets (LLJ), extreme wind shear (EWS), extreme wind veer, and land/sea breezes. These phenomena, in turn, cause a wide range of wind conditions and a significant deviation from the classical description of well-mixed ABL conditions (e.g. Monin-Obukhov similarity theory, power law). Offshore field observations, which serve as a key to both an understanding of complex physical phenomena and model validation in such complex areas, pose a major challenge (Hasager et al., 2008; Sempreviva et al., 2008). The advent of fixed and floating profiling LiDAR technology has enabled an unprecedented step in probing the MABL. However, the measurement range of a profiling LiDAR remains within the first 200-300 m of altitude, which is too restrictive for understanding the aforementionned complex atmospheric flow phenomena and their interactions with wind turbines featuring increasing rotor diameters. The need for more offshore field data near the coastline and covering a higher range of altitude remains one of the current major challenges raised by Veers et al. (2019) and Shaw et al. (2022).

Previous studies involving field observations (using either LiDAR or metmasts) or simulations, as summarized in Shaw et al. (2022), point out the presence of LLJs in the coastal zone (Smedman et al., 1993; Mahrt, 1999; Pichugina et al., 2012; Emeis, 2014; Soares et al., 2014; Mahrt et al., 2014; Nunalee and Basu, 2014; Pichugina et al., 2017; Wagner et al., 2019; Kalverla et al., 2019; Debnath et al., 2021; Djath et al., 2022; Aird et al., 2022; Rubio et al., 2022). LLJs are defined by local velocity peaks in the vertical profile near the ground with a core observed at levels between 50 m from the surface up to more than

500 m. Such a phenomenon often generates high shear and seems to be highly correlated with the stable thermal stratification and/or the coastal transition (topography, heat capacity, etc.) (Soares et al., 2014; Svensson et al., 2019). The precise physics of LLJ formation in the coastal environment appear to be multi-factorial and remains unclear in many situations, thus making it difficult to deduce common characteristics. One common feature observed both in the North Sea (Kalverla et al., 2019) and along the east coast of the U.S. (Aird et al., 2022) is the rate of appearance of LLJs at the coast: in most instances, this rate was found to lie below 15% with a seasonal peak observed at the end of spring. The complexity of modelling an LLJ near the coast through meso-scale simulations was indicated by Nunalee and Basu (2014) and Svensson et al. (2019), wherein the presence and intensity of LLJs were found to be underestimated and model dependent. Since LLJs can occur at the operating altitude of an offshore wind turbine, several consequences, such as a modification of the load distribution on the rotor, wake recovery rate, and turbulence level, would be expected to affect both overall wind turbine performance and structural life cycle, thus making a study of their characteristics significantly important in coastal wind energy projects. To date, offshore and coastal LLJs have mainly been studied in the North and Baltic Seas, closed seas, and along the northeastern coast of the U.S. Their presence along the northwestern European Atlantic coast has remained largely unstudied.

The expected height of next generation offshore wind turbines has ushered in a need to measure wind conditions up to 400-500 m, as these data will be key to the parameterization of offshore wind profiles above the surface layer. Yet such a challenge is one that current profiling Doppler LiDARs cannot handle. Over the past few years, several test campaigns have deployed a scanning LiDAR (sLiDAR) to exploit its larger range to measure wind speed at higher altitudes. Wagner et al. (2019) used a sLiDAR on the FINO1 platform in the North Sea in DBS mode (vertical profiling) to probe up to 518 m. Although data availability was very low (11.9%) due to time-discontinuous LiDAR measurements and partial instrument failure, these authors successfully analyzed LLJ events within a one year period and provided tentative explanations for their generation. At the site, LLJs were detected 14.5 % of the time and on 64.8% of the days. Cheynet et al. (2021) used an sLiDAR in fixed line-of-sight (LOS) regime at a fixed elevation angle and discussed the vertical profile of the radial wind speed (RWS) along the LOS. However, the serious limitation of this approach was that the vertical profile was being measured over a large horizontal distance (several kilometers) without the possibility of verifying horizontal homogeneity. Shimada et al. (2020) and Shimada et al. (2022) successfully validated a method using a sLiDAR from the shore to probe the horizontal wind speed (*HWS*) at a single height above the water surface using a PPI (Plane Position Index) scan. Their experiments were promising, yet further efforts are still needed to measure reliable vertical profiles of the *HWS* near the coast.

The present paper proposes an original method of assessing a high-altitude (500 m) and high-resolution (27 altitudes) wind profile above sea level using a sLiDAR. Based on the work of Shimada et al. (2020), who used an sLiDAR installed at the shore, the method herein is extended from a single height to multiple heights thanks to several PPI scans at various elevations as well as to an increased vertical resolution approach relying on a horizontal homogeneity hypothesis. Our new method employs a selected set of additional measurement gates along each scan, which otherwise had been disregarded during the raw data processing, in order to both expand the vertical range of the wind profile upwards and refine the measurement grid. The hypotheses underlying this method, which include statistical convergence and horizontal homogeneity, are also discussed, notably in the context of wind direction sensitivity. The method was subsequently implemented during a 7-month measurement

campaign on France's west coast, in providing the first dataset and analysis of its kind along the northwest European Atlantic coast. A statistical analysis of LLJs and shear events is also performed to contribute to better understanding their role in the scope of local coastal wind resource. This paper addresses several scientific and technical challenges identified in both Veers et al. (2019) and Shaw et al. (2022) by: (i) proposing an original field experimental method to measure the MABL profile up to 500m with high vertical resolution, (ii) providing a unique dataset in a coastal environment along the northeastern European coast, and (iii) contributing to the quantification of the impacts from LLJs and high shear events for the wind energy sector within a geographical region never before described.

The method, including the original sLiDAR set-up and data processing, is described in Sect. 2. The results, encompassing statistics on LLJs, wind shear events, and power production of 10 MW, 15 MW, and 22 MW turbines over the covered period are presented in Sect. 3. Sect. 4 discussed the results, and a conclusion is provided in Sect. 5.

2 Methodology

Although several wind turbines will be considered in Sect. 3.6, the *IEA 15* MW *240 RWT* [1] wind turbine has been chosen as the reference throughout the analysis herein; it features a 240 m rotor diameter and a hub height of 150 m.

2.1 Field experiment set-up

During the period between March and September 2020, an sLiDAR (Vaisala WindCube Scanning LiDAR 100S) sourced from the Research Laboratory in Hydrodynamics, Energetics and Atmospheric Environment was deployed along the coastline of Le Croisic peninsula, in northwestern France, at a height of 21 m above mean sea level, on the balcony of a seafront villa (Fig. 1). At 100 m from the coastline, and with a clear view of the Northeast Atlantic Ocean from 135° to 260°, this set-up was intended to measure wind conditions above the ocean several kilometers offshore (see Fig. 1, left). A detailed description of the surroundings of this sLiDAR can be found in Paskin et al. (2022) who performed a field experiment in the same environment.

Pitch and roll angles of the sLiDAR were adjusted using internal inclinometers with an uncertainty of 0.1°. The hard-target procedure was performed using a reference vertical pylon situated 550 m from the sLiDAR and equipped with a horizontal beam. While pointing to the reference pylon, a direct and indirect scan crossing the horizontal and vertical beams revealed no backlash greater than 0.05° for both azimuth and elevation directions. A precise measurement of the position and altitude of the pylon, the horizontal beam, and the sLiDAR was carried out using Global Navigation Satellite Systems (GNSS) positioning with a Real Time Kinematic correction (RTK). This measurement served both to adjust the azimuth (ϕ) angle to the North, with an uncertainty of 0.5°, and to estimate the remaining elevation error. For the applicable range of azimuth angles, this error was computed based on the pitch/roll angles given by the sLiDAR and then double-checked by means of external inclinometers. The mean offset (-0.07°) was included in the elevation correction, and the remaining altitude variation along the 45°-wide measuring range was found to equal $\pm 0.07°$, thus corresponding to ± 1.1 m per kilometer distance from the sLiDAR (the correspondence between mean offset and altitude variation within the measurement range remains random). The tide at the site

[1] https://github.com/IEAWindTask37/IEA-15-240-RWT, last access: 10 jun 2024

Table 1. Configuration of the PPI scans in the sLiDAR.

Scan	Azimuth ϕ [°]	Rot. Speed [$^\circ s^{-1}$]	Dir. Rot. [-]	Elevation θ [°]	Acc. time [s]	Duration [s]	Distance of the gate center [m]
PPI1	157.5 - 202.5	3	direct	0	1	15	R = [100 - 3000] each 100 m
PPI2	202.5 - 157.5	3	indirect	0.57	1	15	R/($\cos\theta$)
PPI3	157.5 - 202.5	3	direct	1.72	1	15	R/($\cos\theta$)
PPI4	202.5 - 157.5	3	indirect	4.01	1	15	R/($\cos\theta$)
PPI5	157.5 - 202.5	3	direct	6.32	1	15	R/($\cos\theta$)
PPI6	202.5 - 157.5	3	indirect	13.89	1	15	R/($\cos\theta$)

Rot. Speed: rotation speed; Dir. Rot.: direction of rotation; Acc. time: accumulation time.

(semi-diurnal with a maximum range of +/-2.7 m) was not accounted for in this study; all heights are given above mean sea level.

The sLiDAR was configured to perform a series of six 45° azimuth opening PPI scans at six elevation angles (θ) above the sea surface within the southern sector (denoted PPI1 to PPI6 in Table 1). The direction of rotation was alternated between clockwise and counterclockwise in order to minimize the time between measurements. The total cycle of 6 PPI lasts 96 seconds including moving time without measurement. For the horizontal scan (PPI1 in Table 1), the radial wind speed (RWS) was measured at 30 gates which had been established evry 100 m from 1000 m to 3000 m along the laser beam. The range location of the other PPI scans was obtained by dividing the PPI1 ranges by $\cos\theta$ so as to achieve a vertical alignment of the measurement points at prescribed distances from the sLiDAR (see Fig. 3). The gate size was set at 50 m. All configuration details are given in Table 1. In this work, like in Gryning and Floors (2019) and Paskin et al. (2022), the minimum carrier-to-noise ratio (CNR) threshold value used to validate an RWS measurement was set at -29dB. No upper CNR threshold was applied. All RWS measurements over 30 $\mathrm{m/s}$ and below -30 $\mathrm{m/s}$ were discarded since they exceed the maximum wind speed measurement given by the manufacturer.

2.2 Virtual mast reconstruction approach

Shimada et al. (2020) demonstrated the validity of the horizontal wind speed and direction reconstruction at a single point from a PPI scan through comparison with a fixed profiling LiDAR. Their approach was based on the homogeneity of the wind within the PPI scan. This section proposes using this same reconstruction method (Sect. 2.2.1) but to extend the methodology to obtain a profile reaching 500 m with higher vertical resolution. For this purpose, PPI scans were performed at 6 elevation angles and repeated 6 times within a 10-min period. A profile reconstruction method, discussed in Sect. 2.2.2 is being proposed based on horizontal homogeneity, while Sect. 2.2.3 focuses on the statistical convergence of this approach.

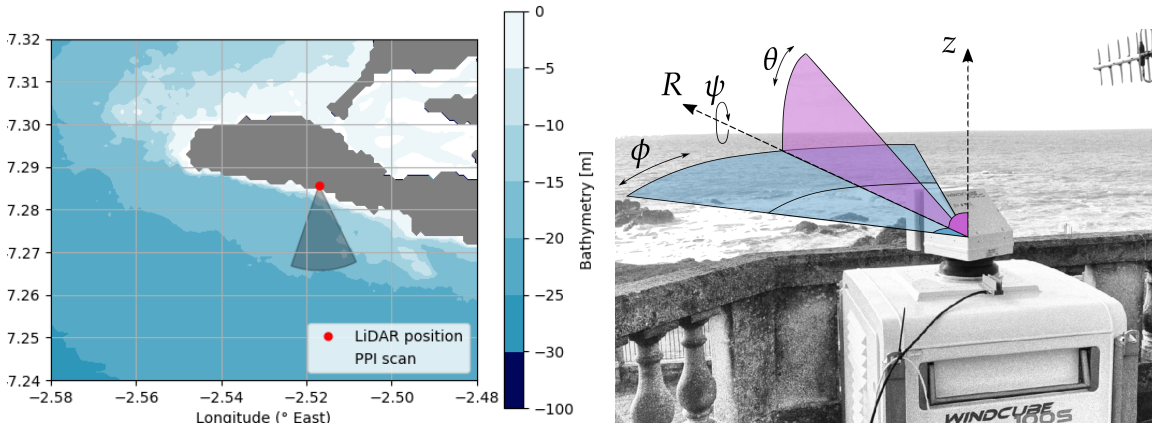

Figure 1. Position of the sLiDAR (red dot) and scanned area (shown in gray) on the peninsula of Le Croisic, France (left). View of the sLiDAR facing the Atlantic (right). Definition of the sLiDAR frame with the azimuth (ϕ) and elevation (θ) angles. This figure has been extracted from Paskin et al. (2022).

2.2.1 Horizontal wind speed estimation

Horizontal wind speed (*HWS*) can be defined either by its eastward and northward components (u, v) or else by (U_h, *DIR*), where $U_h = \sqrt{u^2 + v^2}$ is the modulus of *HWS* and *DIR* is the wind direction. The vertical wind component is denoted by w. During a given scan, each RWS value measured by the sLiDAR at a given gate is related to the wind speed vector components (u, v, w) by

$$RWS = u\ \cos\theta\ \sin\phi\ +\ v\ \cos\theta\ \cos\phi\ +\ w\ \cos\theta\ . \tag{1}$$

In assuming that w is negligible compared to (u,v), which is likely to be the case above the sea surface, Eq. 1 simplifies to

$$RWS = u\ \cos\theta\ \sin\phi\ +\ v\ \cos\theta\ \cos\phi\ . \tag{2}$$

In assuming an homogeneous wind field in both space and time during a single PPI scan, the *HWS* components can be determined by a linear-least-squares method where θ, ϕ and RWS are the known values and (u, v) the unknowns. Shimada et al. (2020) successfully validated this method (called velocity volume processing) versus a profiling LiDAR in a very similar set-up (sLiDAR at the shore measuring over the sea). They reported an accuracy in the *HWS* estimation at 100m above sea level of 0.5% with a determination coefficient of 0.998. Additionally, the elevation angle was reported as having no influence on accuracy. In the present work, a similar approach has been used except that Eq. 2 has been re-written as

$$RWS^* = \frac{RWS}{\cos\theta\ \sin\phi}\ =\ u\ tan\phi\ +\ v\ , \tag{3}$$

so that the fitting is based on a linear regression procedure instead of fitting a sum of sinus functions. In this case, linear regression will yield u as the slope of the $RWS^* = f(\tan\phi)$ line and v as its intercept. Results were verified against the original method of Shimada et al. (2020). This approach displays a limitation in that the variables in the denominator possibly lie close to zero. However, for the sLiDAR setting used in the measurements (see Table 1) neither of the two functions assumes near-zero values at any point. Should a different range of azimuth angles ϕ be used, additional steps would be necessary to avoid division by zero (a simple rotation of the coordinate system before and after fitting could serve this purpose). Moreover, to ensure adequate performance of the algorithm, it is important for the $\tan\phi$ values to be distributed quasi-linearly across the range, i.e. the range of azimuth angles of the sLiDAR setting must lie within the linear part of the $f(x) = \tan x$ graph (which is true in our case).

The quality of the data obtained from the linear regression of Eq. 3 has been assessed by means of a customized quality index (*QI*), based on the Normalized Root Mean Square Error (*NRMSE*). *NRMSE* is obtained by normalizing the ordinary Root Mean Square Error (the standard deviation of the residuals) by the maximum absolute value of the measured RWS^*. The quality index is then defined as the difference between unity and *NRMSE*:

$$QI = 1 - \frac{1}{max(abs(Y_i))}\sqrt{\frac{\sum_{i=1}^{N}(Y_i - \hat{Y}_i)^2}{N}}, \tag{4}$$

where Y_i denotes the measured value of RWS^*, $\hat{Y}_i$ the value predicted by the linear regression, and N the total number of points. The choice of normalization accounts for possible negative or near-zero values of Y_i. In this manner, the calculated wind speed values with a *QI* close to 1 are considered to be of high quality. Data with $QI < 0.75$ are considered unreliable and discarded. After filtering, the u and v values obtained are averaged over 10-minute intervals for each measurement height.

The location of the current measurements near the land-sea transition raises the question of the effect of wind direction on the validity of the hypothesis of spatial homogeneity within each individual scan used to compute *HWS* and *DIR*, especially in the case of wind coming from land. Let's define here and for the remainder of the paper *sea wind* and *land wind* to denote winds coming from the sea [135°-315°] and from the land [315°-135°], respectively (Fig. 10). In Fig. 2, the evolution in the *QI* is given for 15° wind direction bins, along with the number of occurrences in each bin. On the whole, *QI* varies between 0.94 and 0.98, thus indicating a high level of homogeneity within the scanned area. However, a dependence on wind direction is indeed visible since we observe a lower *QI* for *land wind* (0.96) compared to *sea wind* (0.97).

Another source of uncertainty in the *HWS* estimation visible in Fig. 2 pertains to the relative wind direction compared to the main scan pattern direction: a primary wind direction oriented across the mean LOS of a scan (across-LOS) results in less accurate measurements due to RWS measurements of near zero, compared to situations in which the wind direction is along the mean LOS of the scan (along-LOS), whereby the RWS represents most of the wind speed amplitude. This effect is expected to lower the quality of the *HWS* determination as reported in the literature in (Cameron et al., 2014; Shimada et al., 2020). According to Simon (2015), a scan range wider than 30° is expected to limit this problem. For the present study, in the absence of a reference measurement, this alignment effect has been evaluated in Fig. 2 by comparing the *QI* for the along-LOS and across-LOS directions. The effect is visible with, a mean *QI* of 0.975 and 0.945 for the along-LOS and across-LOS,

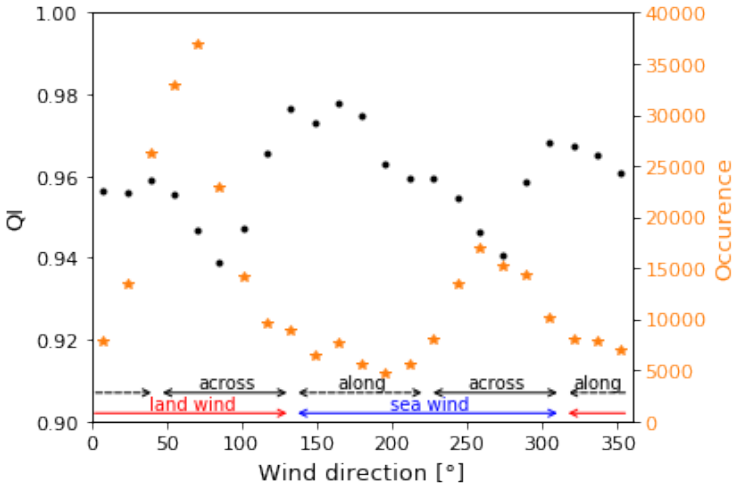

Figure 2. Quality index as a function of wind direction. The relative direction across or along refers to the mean LOS of the scan. The number of observations in each bin has been given for information purposes.

respectively. This difference, similar to the results found in Cameron et al. (2014) and Shimada et al. (2020), is expected to have little effect on the interpretation of our results.

Performing the scans across the most frequent wind directions might appear to be counterintuitive, but the reason for choosing this configuration was to achieve a maximum distance of scanning into the sea, thereby ensuring maximum homogeneity within each scan. Scanning across the shoreline, with all the inherent complex atmospheric processes, is expected to have a strong effect on homogeneity and thus increase measurement uncertainty. Fig. 2 shows that homogeneity is indeed satisfactory and the measurements can be considered valid.

In the absence of a local wind reference, an analysis of the *QI* provides relative uncertainty estimates that seem to be reasonable for analysing the wind profiles.

2.2.2 Vertical profile reconstruction and 10-min averaging

Throughout the measurement campaign, the six PPI scans defined in Table 1 and displayed in Fig. 3 are performed one after another in a loop, amounting to a total of 6 scans of each elevation angle within a 10 minute interval. From each scan and for each useful gate, the instantaneous wind components are extracted through the linear regression algorithm described above, with the values obtained then being averaged over 10 minutes. Each scan is associated with pre-configured measurement gates, i.e. distances from the sLiDAR along the scan at which the RWS is recorded (gray circles in Fig. 3). The elevation angles and gates are laid out in such a way that at the target distance from the sLiDAR (here 1400 m), the Nth gates of all six scans are vertically aligned, thereby creating a “virtual met mast” (orange circles in Fig. 3). The six measurement heights of this mast are 0, 14, 42, 98, 155 and 346 m above the sLiDAR (which is located at 21 m above mean sea level). The choice of distance

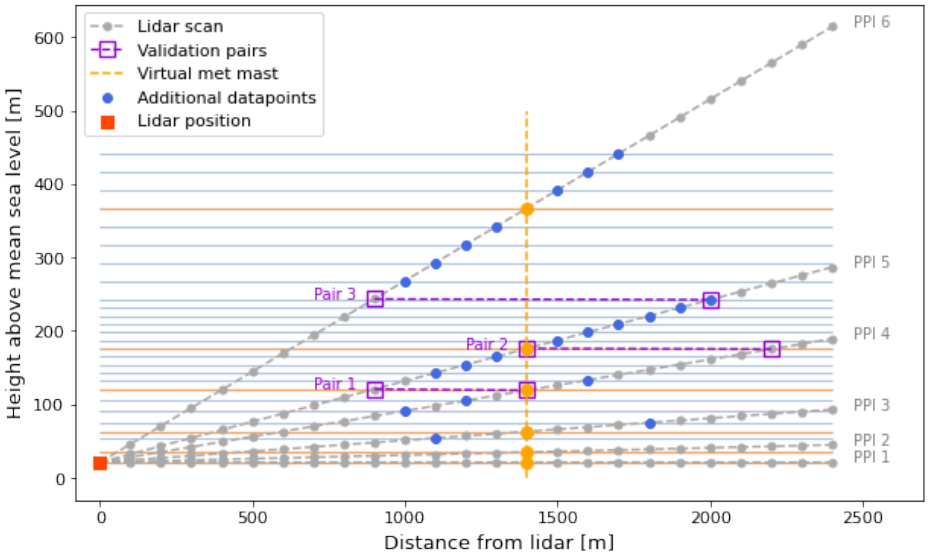

Figure 3. Representation of the elevation of measurement points along the PPI scans (gray dotted lines). The location of the reconstructed mast is marked in orange. The blue dots denote the additional points taken into account during this reconstruction approach. The purple squares are comparison points, at the same height, used for validation.

for the virtual mast reconstruction strikes a compromise between being far enough from the shore while maintaining a high CNR that decreases with distance from the LiDAR.

The novel part of the methodology presented herein is aimed at ensuring improved height resolution of the vertical profile by making use of the other measurement gates along each scan, which otherwise would be disregarded. For this purpose, RWS measurements from the gates adjacent to those forming the virtual met mast are included in the dataset (blue circles in Fig. 3), thus adding 21 new measurement heights (33, 54, 70, 84, 112, 122, 133, 144, 166, 177, 188, 199, 210, 221, 253, 276, 300, 323, 369, 393 and 416 m above the sLiDAR). These additional heights extend the mast further upwards and provide significant grid refinement at altitudes more than 100 m above the sLiDAR. Such an expansion relies on the assumption that variations in wind properties are much more pronounced with height than with distance from the shore within the new mast "width". To validate this assumption, three validation pairs (shown in purple in Fig. 3) were selected, whereby wind speed and direction are compared at the measurement points with the same height but a different distance to the shore. Pairs 1 and 2 compare the conditions at the boundaries of the extended mast with those at its core, while Pair 3 spans the entire extended width. The results of this comparison are presented in a scatter plot in Fig. 4, which reveals a good correlation in both *HWS* and *DIR* for each pair. Despite the land-sea roughness and thermal transition due to the coast, the evolution in horizontal wind is not significant within a 1000 m horizontal range centered at the virtual met mast for the tested height, thereby verifying the horizontal homogeneity (for purposes of this particular study). As a comparison, the horizontal evolution lies on the order of 1% for 1000 m where the vertical gradient of *HWS* is about 10% for 100 m. Let's note that the two measurements in each pair have not been performed

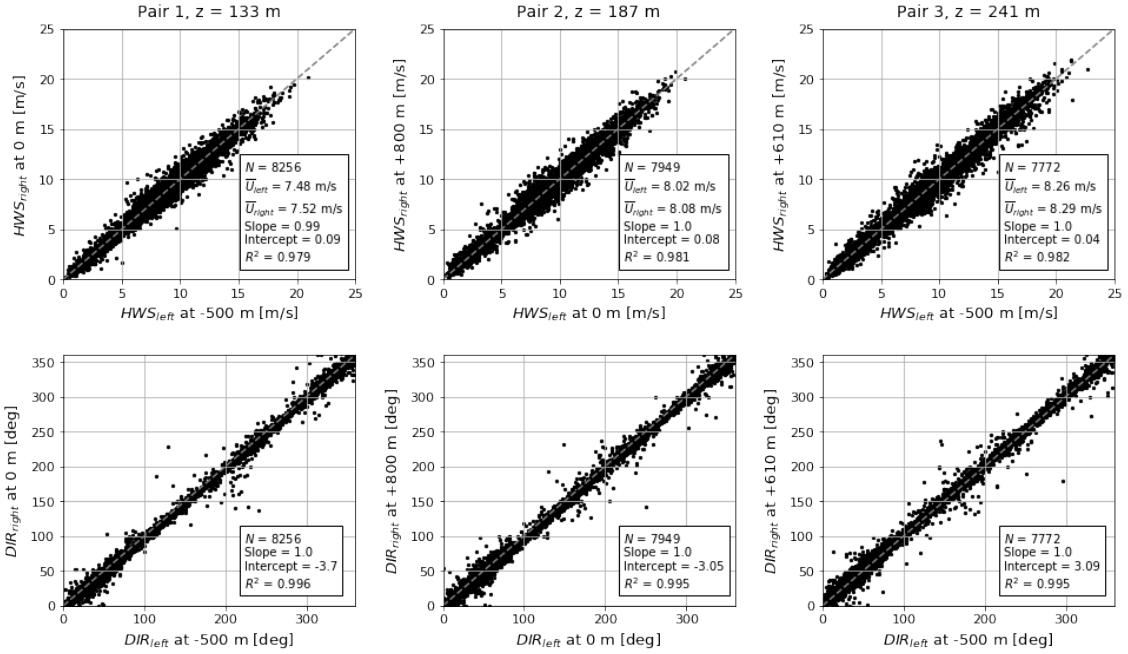

Figure 4. Horizontal wind speed and wind direction comparison for three validation pairs. Axis labels provide the distance of each measurement point (left and right) from the virtual mast.

exactly simultaneously, hence the measured wind speeds are not expected to perfectly match in a turbulent flow and, are thus expected to increase the scatter in Fig. 4. The underlying assumption of the increased height resolution method can therefore be considered as valid, and the method is employed for the subsequent analysis, allowing for a more detailed vertical description of the MABL.

The profiles obtained are further subjected to reliability filtering, whereby a profile is considered reliable if more than 5 valid measurements are available within the 10-minute averaging interval for at least 20 heights out of the 27. The unreliable profiles are not to be used for any further analysis. Overall, 81.4% of all profiles are considered reliable.

Proximity to the coastline again raises the question of the directional influence on homogeneity over the distance used in the reconstruction methodology. The correlation coefficient R^2 between the two measurements at the three comparison heights of Pairs 1-3 are presented as function of the wind direction in Fig. 5 to serve as a homogeneity indicator. The highest value (close to 1) is achieved under *sea wind* conditions and when the scan is along the wind direction. The correlation drops to 0.97 for the *land wind* sector and the coefficient becomes height-dependent. The lowest value is found for *land wind* when the wind direction is across-LOS; this value proves to be the lowest among all altitudes studies. The height dependency is likely related to the land/sea transition as well as to the higher shear exponent typically occurring above land. The effect of wind direction either across or along the LOS is visible, with the same order of magnitude as in Fig. 2. This analysis demonstrates the limitation of this method, which is more effective over sea than in the land-sea transitions.

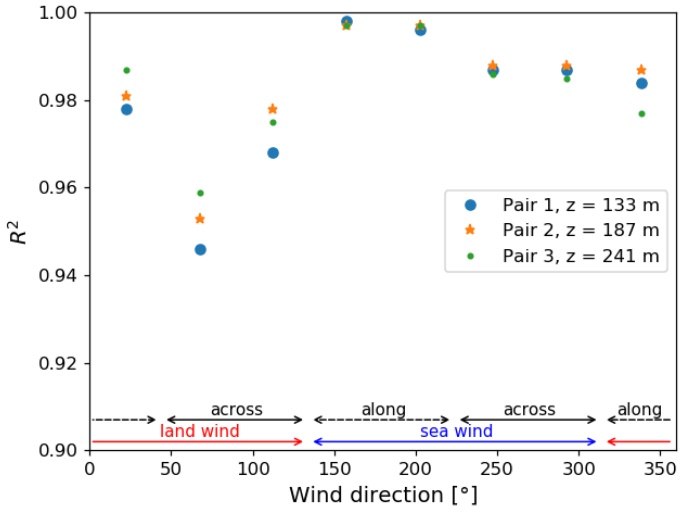

Figure 5. Correlation coefficient R^2 between the two measurements of each pair as a function of wind direction by 30° wind sector.

2.2.3 Statistical convergence of the 10-min horizontal wind speed estimation

During a 10-min period, the sLiDAR performs measurements at 6 different heights, thus making it necessary to verify how the statistical convergence of the final 10-min average is affected. Since it is being calculated from a finite signal, U_h measured in the field has a statistical convergence error of $\epsilon_{U_h} = \pm z_{\alpha/2} \frac{\sigma_u}{\sqrt{N}}$, where $z_{\alpha/2} = 1.65$ refers to the 90% confidence level, N is the number of independent samples, and σ_U the standard deviation of U_h. The frequency at which the sLiDAR computes U_h is quite low, i.e. 6 times during a 10-min interval, compared to a one-point measurement such as that using an ultrasonic anemometer (USA) or a cup anemometer for measuring the *HWS* at 20 Hz. However, as opposed to a USA, the sLiDAR also accumulates measurements in space during each PPI, hence time and space are contributing to an increase in N.

In the time domain, following George et al. (1978), the number of independent samples in a time series of duration T is estimated by

$$N = \frac{T}{2T_u}, \tag{5}$$

where T_u is the integral time scale computed from the auto-correlation of the signal. Using the Taylor frozen turbulence hypothesis, in the space domain, measurements are considered to be independent when spaced by two times the integral length scale Λ_u along the wind direction (in this analysis, it is assumed that Λ_u is homogeneous in the horizontal plane). Λ_u can be estimated by $\Lambda_u \approx \kappa z$, with $\kappa = 0.4$ being the von Karman constant and z the height above the sea surface, and in assuming Taylor frozen turbulence (although it is not perfect, (Kaimal and Finnigan, 1994)), plus time and length scales being related by

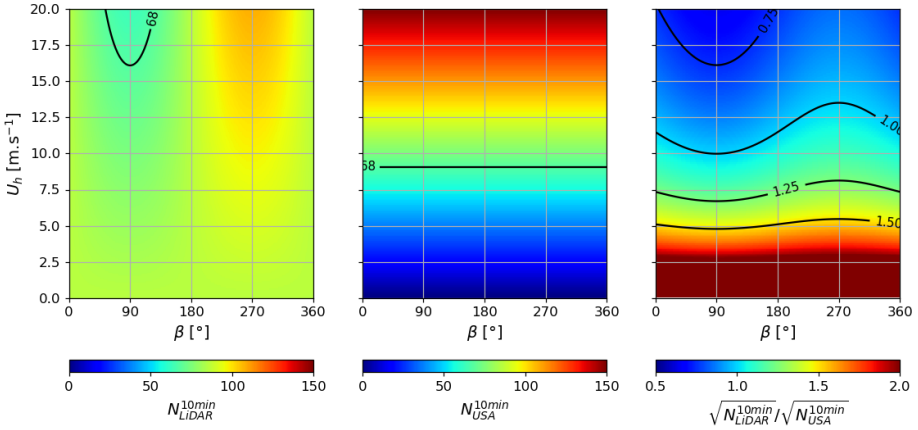

Figure 6. Evolution of N_{sLiDAR}^{10min} (left), N_{USA}^{10-min} (middle) and R_ϵ(right) as a function of U_h and β.

$\Lambda_u = U_h\, T_u$. Here, the maximum number of spatially independent points per scan can be approximated by

$$N_{sLiDAR} = \frac{L_{sLiDAR}}{2\Lambda_u}, \tag{6}$$

where

$$L_{sLiDAR} = L_{scan} - T_{scan} U_h sin\beta \tag{7}$$

represents the equivalent length of one scan and

$$L_{scan} = 2Rsin\left(\frac{\Delta\theta}{2}\right) \tag{8}$$

is the cord of a scan (straight-line distance between the start and end of a scan at a given range), with $\Delta\theta$ being the azimuth opening of the scan and R the distance to the centre of the gate considered. $T_{scan} U_h sin\beta$ is the equivalent distance traveled by the wind in the direction of the scan during the scan duration T_{scan}. β is the direction of the sLiDAR beam relative to the wind (0° indicated that the mean azimuth is aligned with the main wind direction). In the tested configuration, each scan is performed 6 times during a 10-min period leading to a maximum number within a 10-min period of $N_{sLiDAR}^{10-min} = 6\frac{L_{sLiDAR}}{2\Lambda_u}$.

In Fig. 6 (left), N_{sLiDAR}^{10-min} is visualized as a function of β and U_h with $z = 100\ m$, $\sigma_u = 1\ m/s$, $R = 1500\ m$, and $\Delta\theta = 45°$. N_{sLiDAR}^{10-min} is not highly dependent on U_h and varies slightly with β; the most favourable condition is $\beta = 270°$, at which point the scan goes in the direction opposite that of the wind. The value $N_{sLiDAR}^{10-min} = 68$, as marked in the figure, refers to the number of independent points necessary to reach 2% of error a 90% confidence level. For purposes of comparison, a USA placed in the same flow will collect, in 10 minutes,

$$N_{USA}^{10-min} = \frac{600}{2T_u} = \frac{600U_h}{2\Lambda_u} \tag{9}$$

independent samples not influenced by the wind direction. Figure 6 (middle) shows that N_{USA}^{10min} is highly sensitive to wind speed variation. Indeed, the statistical convergence of a single point is solely a function of the number of independent measurements acquired in 10 min under the hypothesis of a time scale independent of wind speed: the higher the wind speed, the higher the number of points measured over a 10 min time interval. In contrast, the sLiDAR can rely on spatial measurements, regardless of the wind speed.

Finally, the ratio of the error produced by the sLiDAR compared to a USA, i.e.

$$R_\epsilon = \frac{\epsilon_{sLiDAR}^{10min}}{\epsilon_{USA}^{10-min}} = \frac{\sqrt{N_{sLiDAR}^{10-min}}}{\sqrt{N_{USA}^{10-min}}}, \tag{10}$$

shown in Fig. 6 (right), becomes independent of Λ_u and σ_u. For low wind speeds, typically $U_h < 10\ m/s$, the sLiDAR provides (in the present configuration) a lower statistical error compared of that of a USA, while the opposite is observed when $U_h > 10\ m/s$. Note that these results would be similar when compared to those of a cup anemometer instead of a USA since only independent samples can be included for to estimate the number of independent points.

When applied to the configuration used in this work (Table 1), the resolution of the PPI scans (15 points in a 45° scanning sector) is sometimes lower than N_{sLiDAR}^{10-min}. In this case, the statistical error is estimated using $N = min(N_{sLiDAR}^{10-min}, 15)$. In our specific distance range, the statistical uncertainty at the 90% confidence level varies within $\epsilon_{sLiDAR}^{10-min}$ = [1.74 - 4.35]%.

2.3 Definition of wind profile characteristics

2.3.1 Shear exponent definition

Throughout the present analysis, wind shear, also called shear exponent, α has been defined according to the power law:

$$U = U_{ref}\left(\frac{Z}{Z_{ref}}\right)^{\alpha}, \tag{11}$$

where U_{ref} and Z_{ref} denote the reference 10-min wind speed and reference height, respectively. This equation can be rewritten in logarithmic form as follows:

$$\log U = \alpha \cdot \log Z + (\log U_{ref} - \alpha \cdot \log Z_{ref}), \tag{12}$$

according to which α can be taken as the slope of the $U(Z)$ function in a log-log scale, hence making it possible to determine the shear exponent value from several wind speed values at different heights using linear regression. The shear exponent is

derived from the wind speed values within the rotor area only (i.e. between the heights closest to the bottom and the top of the reference turbine rotor). This definition was chosen to comply with wind energy related application. Note that a higher shear may be present in the wind profile outside the rotor, such that this choice of definition is tailored to a particular wind turbine. In Sect. 3.3, the rotor shear calculation will be performed for each rotor as part of the data processing step for each valid wind profile.

2.3.2 Low-level jet detection method

In this study, low-level jets are defined as a peak in the vertical wind profile. Atmospheric stability, roughness transition, possible formation mechanisms and spatial extension are not accounted for in the detection process. Detection is performed for every valid 10-minute averaged profile through an algorithm based on the SciPy function `find_peaks` in following a four-step process. In the first step, peaks more prominent than 1 $\mathrm{m/s}$ and not narrower than 5 height levels (assigned so as to exclude sharp fluctuations) were detected. If the function returned more than one peak, the profile was considered not to contain an LLJ. In the second step, both absolute and relative low-level jet criteria were introduced to evaluate the derived maximum, offering a method similar to that described by Aird et al. (2022). The peak was considered an LLJ if it reached 2 $\mathrm{m/s}$ and/or a value 20% (in relative terms) higher than the next profile minimum. The third step, treated the time dimension of low-level jets as a phenomenon. The Boolean array corresponding to LLJ presence or absence was filtered so that an isolated 10-minute averaged profile with a detected LLJ is not accounted for in the final statistics. On the other hand a non-LLJ case surrounded by LLJ-cases on the timeline would be counted as such. The fourth and final step sought to improve the LLJ statistics by detecting low-level jets as a phenomenon spread over time and not just as a feature of isolated profiles. The detection algorithm is able to locate the core of the low-level jet at 25 m or higher with at least a 25 m vertical resolution (although it is not even throughout the profile, Fig. 3).

3 Results

This section presents relevant results describing the wind resource at the coastal site. After a comparison with reanalysis data for validation purposes, the focus squarely placed on LLJ (occurrence, height, core speed, direction, etc.) and extreme wind shear (occurrence, level, direction, etc.) given that these phenomena can be viewed as deviations from the classical wind profile description used for wind turbine design. The 15 MW turbine will be used as a reference in this section except in Sec. 3.6, where several turbines will be used to analyze the energy production statistics.

3.1 Comparison with reanalysis data

In the absence of direct reference measurements nearby, the AROME hourly reanalysis dataset has been used as an independent datasetfor comparison with the *HWS* and *DIR* profiles deduced from the sLiDAR measurements. AROME is a reanalysis product of MeteoFrance [2] with wind data available at 24 heights between 20 m and 3000 m above ground level and with a

[2]https://donneespubliques.meteofrance.fr

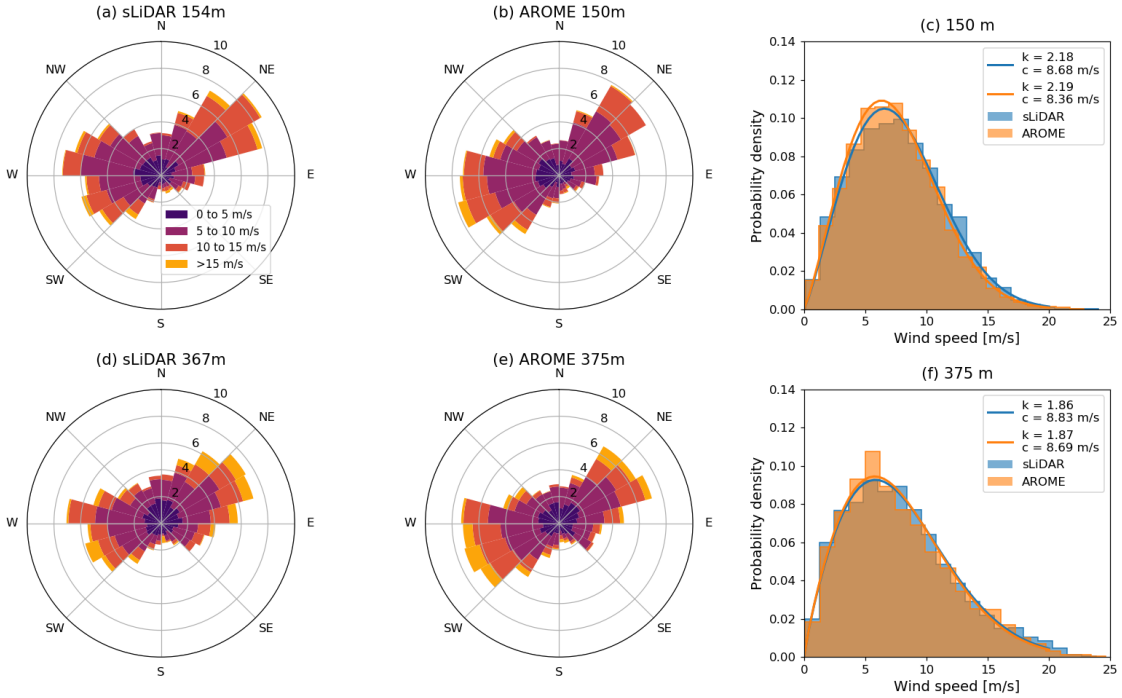

Figure 7. Wind rose and Weibull distribution at 150 m (a, b, c) and 375 m (d, e, f) for the sLiDAR and AROME reanalysis data.

horizontal grid spacing of 0.025° (approx. 2.5 km in the area of interest). This dataset was chosen for its good spatial resolution, which is of particular benefit in our complex coastal area. For starters, two AROME heights, 150 m and 375 m, were selected to draw a comparison of *HWS* and *DIR* with the nearest sLiDAR data (154 m and 367 m). Scanning LiDAR data were then resampled to one hour in order to match the reanalysis data time resolution. Figure 7 (a, b, d, e) shows a high level of agreement between the wind roses based on the sLiDAR and AROME data. Figure 7(c, and e), presents the wind speed distributions of both AROME and sLiDAR for the entire measurement period. The Weibull distribution fit is expressed by:

$$PDF(U_{hub}) = \frac{k}{c}\left(\frac{U_{hub}}{c}\right)^{k-1} e^{-\left(\frac{U_{hub}}{c}\right)^{k}}, \tag{13}$$

where c is the scale parameter and k the shape parameter, as calculated from the measured data using the empirical formulae offered by Justus et al. (1978). Both heights show good agreement and very similar Weibull coefficients. Nevertheless, some differences are visible in the wind speed distribution at 150 m, where the 5-7 m/s range is more probable in the AROME dataset than in sLiDAR observations. In contrast, within ranges 1-5 m/s and 10-15 m/s, more sLiDAR observations are drawn than with the AROME data. At 375 m, the distributions more closely matched with another. To draw a more quantitative comparison, scatter plots for *HWS* (a and b) and *DIR* (c and d) are presented in Fig. 8. Generally speaking, the results show a high level of scatter, which would be expected when comparing local measurements at a complex site in order to reanalyse

data. For the *HWS*, the correlation coefficient is lower at 150 m (0.8) versus 375 m (0.84), yet the fitting slopes are close to unity at both heights. The *DIR* scatter plots (Fig. 8 c and d) show a high level of correlation, i.e. 0.97 and 0.96 at 150 m and 375 m, respectively, with a slope of one.

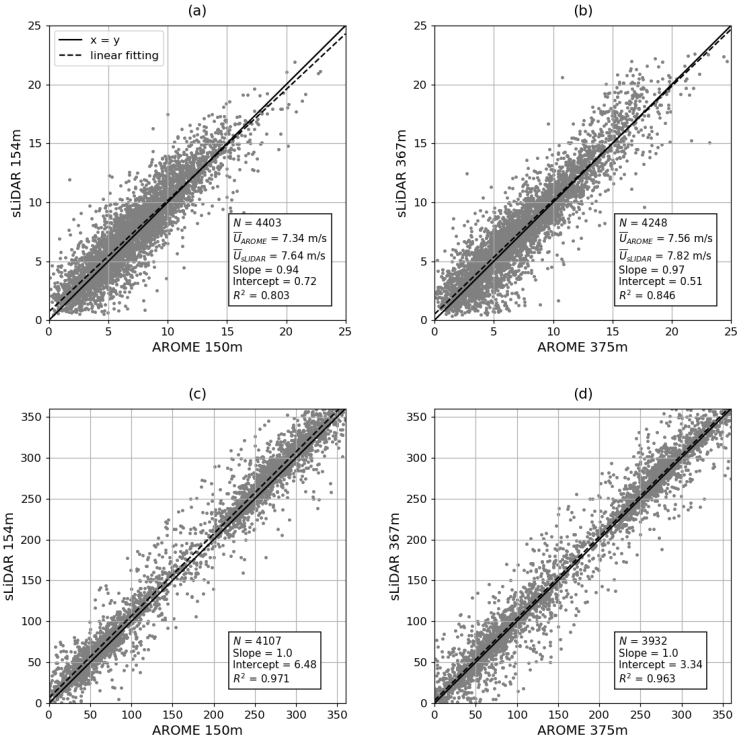

Figure 8. Scatter plot of sLiDAR data vs AROME reanalysis data at 150 m and 375 m above sea level for wind speed (a,b) and wind direction (c,d)

Furthermore, monthly AROME profiles within the first 500 m are compared to the sLiDAR monthly profiles displayed in Fig. 9. The mean AROME profiles have been derived for periods when sLiDAR data were available. For all months, the AROME and sLiDAR profiles appear to be very similar, including September and July, when the mean profile does not resemble a conventional monotonically-increasing wind speed curve. The largest discrepancies are observed locally during summer, in August, when wind speed is at its lowest.

All comparison results show a good level of correlation between sLiDAR data and AROME reanalysis. More discrepancies are observed at the lowest level, which can be explained by the very high complexity of the coastline. Given their spatial resolution and the coastline complexity, AROME reanalysis data have not been adopted herein as a strict reference, but rather as an independent comparative basis to more globally verify that the sLiDAR set-up, measurements and post-processing procedure are not systematically biased.

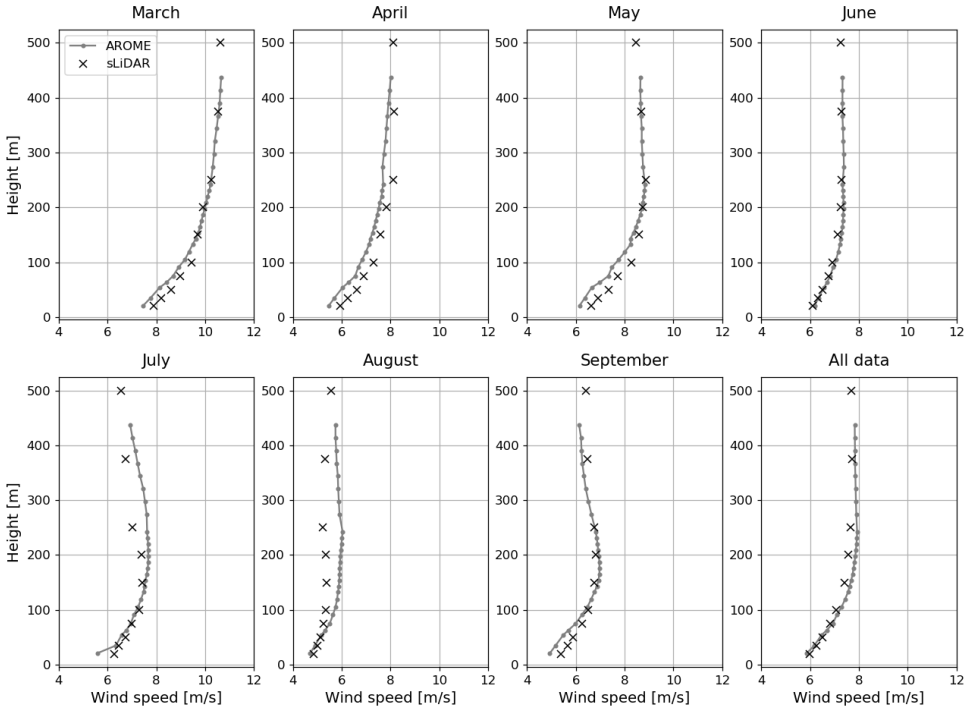

Figure 9. Comparison of the monthly mean profiles of sLiDAR data vs AROME reanalysis data.

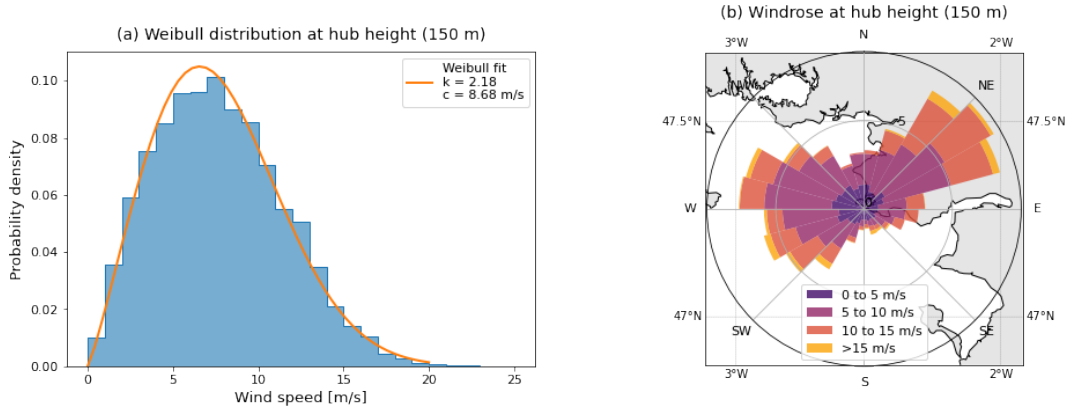

Figure 10. (a) Histogram of the 10-min wind speed at hub height for the entire measurement period with a Weibull fitting (red line); (b) Wind rose of the 10-min wind direction at hub height superimposed on the local coastline with a 15° resolution. The colors correspond to hub height velocity ranges.

	Mar	Apr	May	Jun	Jul	Aug	Sep	Overall
Reliable profiles [%]	91.8	92.5	85.8	94.5	64.0	60.6	81.0	81.4
Maximum wind speed [m/s]	24.0	21.4	19.1	20.8	15.0	20.4	17.1	24.0
Mean wind speed [m/s]	9.7	7.3	8.4	7.3	7.6	5.9	6.9	7.7
Maximum shear exponent	1.38	1.65	1.09	1.46	1.05	1.39	1.24	1.65
Minimum shear exponent	-1.43	-1.58	-1.68	-1.12	-1.35	-1.42	-1.40	-1.68
Mean shear exponent	0.15	0.11	0.13	0.09	0.10	0.07	0.13	0.11
LLJ occurrence [%]	9.0	13.1	18.8	8.0	14.8	16.8	31.3	15.4
LLJ cases	370	524	719	324	424	454	999	3814
Mean LLJ core speed [m/s]	9.5	8.2	10.0	10.1	10.1	8.5	9.3	9.4
Mean LLJ core height [m]	171.6	150.8	157.8	180.3	186.3	177.0	166.8	167.9

Table 2. Monthly and global wind statistics from 10-min data: wind speed at hub height, shear exponent, and LLJs.

3.2 Global wind statistics

Monthly and overall wind statistics, including those on LLJs and wind shear, from the period of the test campaign are given in Table 2. Data availability of the vertical profiles, defined as the ratio between the number of valid profiles and the total possible number of profiles, exceeds 80% for most months. The availability in July and August below 65% is due to periods when the sLiDAR was used for other purposes than the test campaign, as described in this article. Consequently, the statistics for these months should not be taken as fully statistically representative of the period (mean wind speed, number of LLJs detected, etc.). Also, the total database does not cover a full year. For these two reasons, the overall statistics in Table 2 and Fig. 10 are not representative of yearly statistics. The LLJ occurrence rate is calculated as a percentage relative to the number of reliable (valid) profiles. The monthly mean wind speed at hub height (U_{hub}) varies from 5.9 $\mathrm{m/s}$ in August to 9.7 $\mathrm{m/s}$ in March when the site is typically subjected to a series of low-pressure cells generating storms. Fig. 10a presents the 10 min averaged wind speed distribution for the entire measurement period along with the fitting by a Weibull distribution (Eq. 13). The wind rose of 10 min-averaged wind speed at 150 m (Fig. 10b) shows a clear dominance of two wind sectors: western winds in the [200°-315°] sector, likely resulting from Atlantic cyclonic depressions; and northeastern winds in the [0° - 90°] sector. This pattern is typical for the given area, yet should not be considered as an annual statistical representation since the entire winter season and a large part of the autumn are not included in the dataset. Western winds may be underrepresented in the dataset. In the following sections, *sea wind* and *land wind* will be used to denote winds originating from the sea [135°-315°] and land [315°-135°], respectively.

3.3 Wind shear statistics

Monthly averages of α range from 0.07 to 0.15 (Table 2); the average value for the dataset, $\alpha = 0.11$, lies below the values used for offshore (0.14) and onshore (0.2) wind turbine design (IEC, 2009, 2005). However, very large variations are also observed

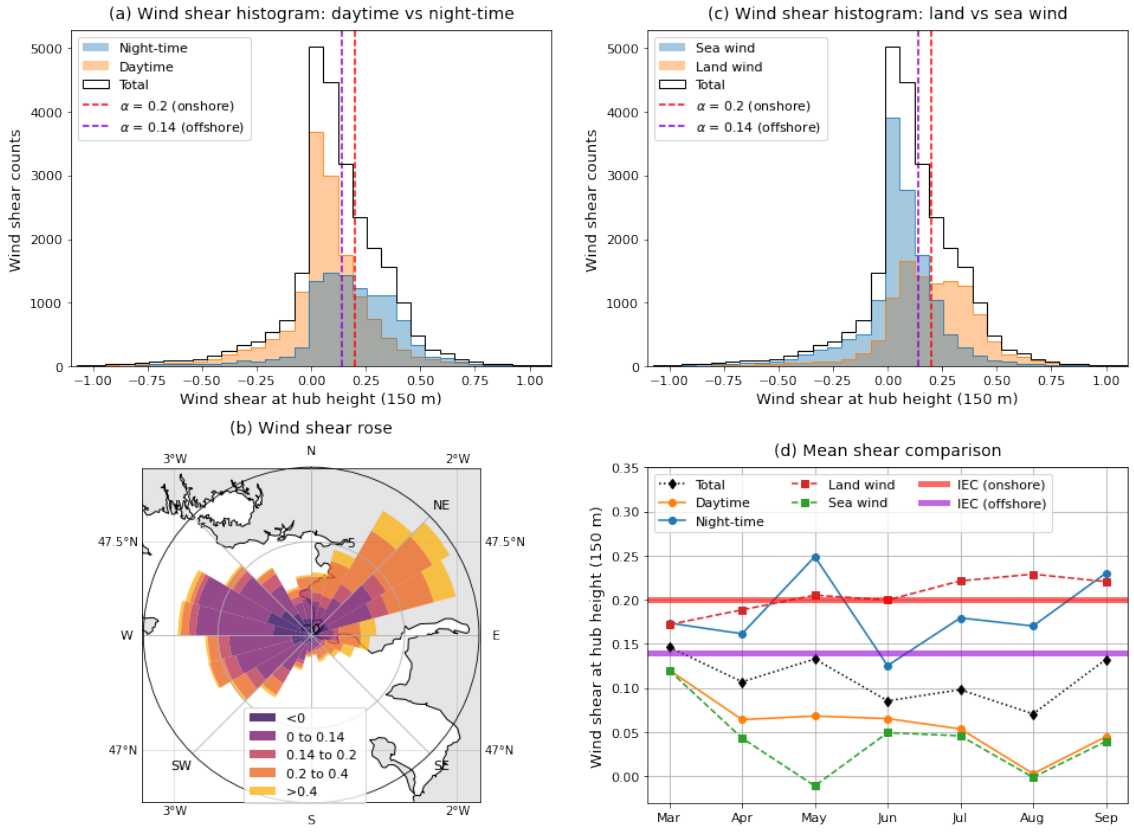

Figure 11. Statistics of the wind shear exponent α. (a) Histograms of α comparing daytime and nighttime. (b) Wind rose of α. (c) Histograms of α comparing wind direction sectors (sea wind and land wind). (d) Monthly averages of α in different categories.

over the entire period, extending to levels above 1 and below -1, as seen in Fig. 11a. The overall wind shear distribution, shown as a black contour, exhibits considerable scattering around the mean value with a thicker tail towards higher values. The sub-distribution corresponding to *daytime* (orange in the figure) is more symmetrical with a sharp peak around a lower shear value ($\alpha \approx 0.06$), while the *nighttime* distribution (blue in the figure) is shifted towards higher values ($\alpha \approx 0.2$) with more spreading, thereby creating the thick tail in the overall distribution. *Daytime* and *nighttime* are defined by the astronomical sunrise and sunset times, respectively.

Figure 11b presents histograms of α with a wind direction filtering. We observe that land winds are associated with higher wind shear than sea wind. Since the shear coefficient over land is higher than at sea, results indicate that for land wind, at the LiDAR location, the wind shear displays characteristics resembling the land.

Figure 11c provides the distribution of α broken down by 15° wind direction sectors in a wind rose format. This distribution shows that *land winds* tend to bring higher wind shears compared to *sea winds*. A high α is clearly associated with onshore conditions meaning that some inland wind characteristics persist out from the shore, at least up to 1.5 km.

Figure 11d presents the monthly average values of α all the four categories (*sea wind*, *land wind*, *nighttime* and *daytime*). Once again, a significant difference is observed between categories, with *daytime* and *sea winds* values lying well below the IEC offshore shear reference of 0.14, and for the most part below 0.1, in heading down into to negative values in May. Their *nighttime* and *land wind* counterparts are much higher and, in some cases, lie above the IEC onshore shear reference of 0.2.

	NWS	**LWS**	**MWS**	**HWS**	**EWS**
Ranges	$\alpha \leqslant 0$	$0 < \alpha \leqslant 0.14$	$0.14 < \alpha \leqslant 0.2$	$0.2 < \alpha \leqslant 0.4$	$\alpha > 0.4$
Time share	14.2%	45.6%	10.9%	23.0%	6.3%

Table 3. Definition of the wind shear ranges and proportion of time spent in each range.

Five ranges of α are given in Table 3 for the purpose of defining the wind shear, namely: negative wind shear (NWS), representing situations where the wind speed is monotonically decreasing with height; low wind shear (LWS), with positive values below the IEC reference for offshore; medium wind shear (MWS), with values between the offshore and onshore IEC references; high wind shear (HWS) when α surpasses the IEC onshore reference; and lastly extreme wind shear (EWS), where α is more than twice the onshore IEC reference.It can be seen in Table 3, which lists the shares of time spent in each range, the LWS and MWS ranges, both in agreement with IEC standards, when combined, represent approximately 56.5% of the total observation time. Higher shear is observed for nearly 30% of the time (HWS and EWS), including over 6% of extreme wind shear. NWS events are not negligible, with a 14% share.

3.4 Low-level jet statistics

For illustration purposes, an LLJ event that took place during the night of May 26th and 27th, May 2020 is shown in Fig. 12 in the form of a color map, where time (with 10 min steps) and height above sea level are shown on the horizontal and vertical axes, respectively, and the color scale depicts wind speed. The narrow strip under the color plot marks daytime (white) and nighttime (blue) periods, while the hatched area corresponds to the reference wind turbine rotor (15 MW). The LLJ can be clearly seen as a yellowish formation starting at sunset with a core moving down to a height of 200 m above the MSL around the middle of the night and rising back during the early morning. On the right side, the wind profile presented exhibits high wind shear in the rotor area, a small peak near 200 m high and a flatter profile above.

In examining global statistics, LLJs detected using the method introduced in Sect. 2.3.2 are observed 15.5% of the time during the experiment (based on valid profiles). Their mean core speed equals 9.4 $\mathrm{m/s}$ and their mean core height is 168 m. As illustrated in Table 2 and in Fig. 13, their occurrence, height and strength vary by month, wind direction and time of day.

Figure 13a presents the number of occurrences of LLJ-featuring profiles as a function of time of the day; it can be seen that the occurrence rate reaches a peak at night, very low between 10 am and 3 pm, and increasing after 3 pm towards the evening in a clear diurnal pattern. The graph confirms that low-level jets are more prevalent in the nighttime during the observed period.

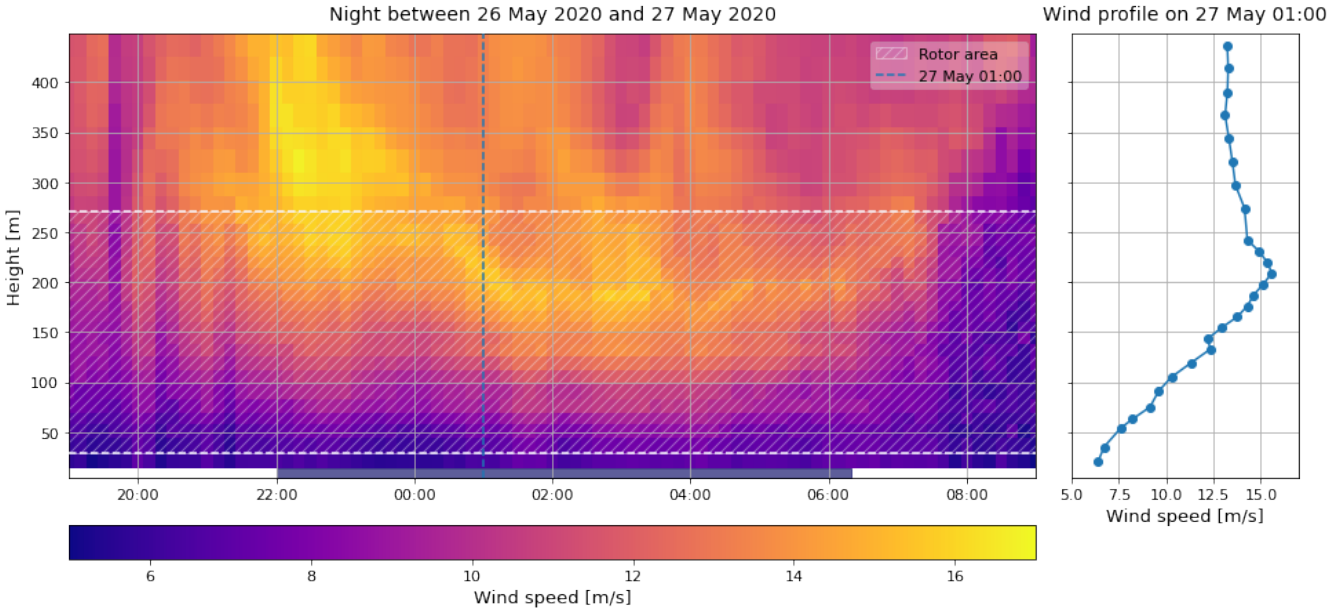

Figure 12. Illustration of a low-level jet event during the night of May 26th to 27th, 2020. The hatched area represents the rotor area. On the left, horizontal wind speed is depicted in the form of a color map as function of time and height above mean sea level. On the right, a 10-min profile at 01:00 illustrating a LLJ is shown.

Figure 13b shows the distribution of LLJs by wind direction, while the color scale indicates wind speed at the LLJ core. Most of the LLJs (58.4%) are coming from the [15° - 90°] wind sector, thus corresponding to a *land wind*. A significantly smaller proportion (19.7%) originates from the northwest direction, roughly blowing along the coastline.

Figure 13c offers the distribution of LLJ core speed for the entire dataset (black line) and two sub-distributions corresponding to *daytime* and *nighttime* occurrences of LLJs (orange and blue histograms, respectively). The *nighttime* distribution displays a significantly wider spread than that of the daytime and is shifted towards higher speeds. In the plot, the gray histogram reflects the hub height wind speed distribution, like in Fig. 10a, for comparison purposes. Note that this histogram has a different vertical scale (on the right), because LLJ events are only detected in a small portion of all profiles. It can also be seen that the general distribution is similar, in shape, to the *daytime* LLJ core speed distribution; however, the *nighttime* LLJ core speed histogram is shifted to the right by about 3-4 m, meaning that wind speeds in LLJ cores are, on average, higher than those at the hub height (at least for this reference turbine during the experiment).

Figure 13f illustrates the monthly variability of LLJ core speed in the form of a boxplot, with the width of the boxplots proportional to the LLJ occurrence for each month (as a visual reference, see Table 2 for the exact values). The structure of the boxes follows a classical boxplot approach widely used in statistics, whereby, the notched "waist" corresponds to the median value of the set, the box itself extends from the first to the third quartile, the whiskers reach the furthest data points within 1.5x of the inter-quartile range, and the circles represent the remaining data points (outliers). The monthly mean wind speed is

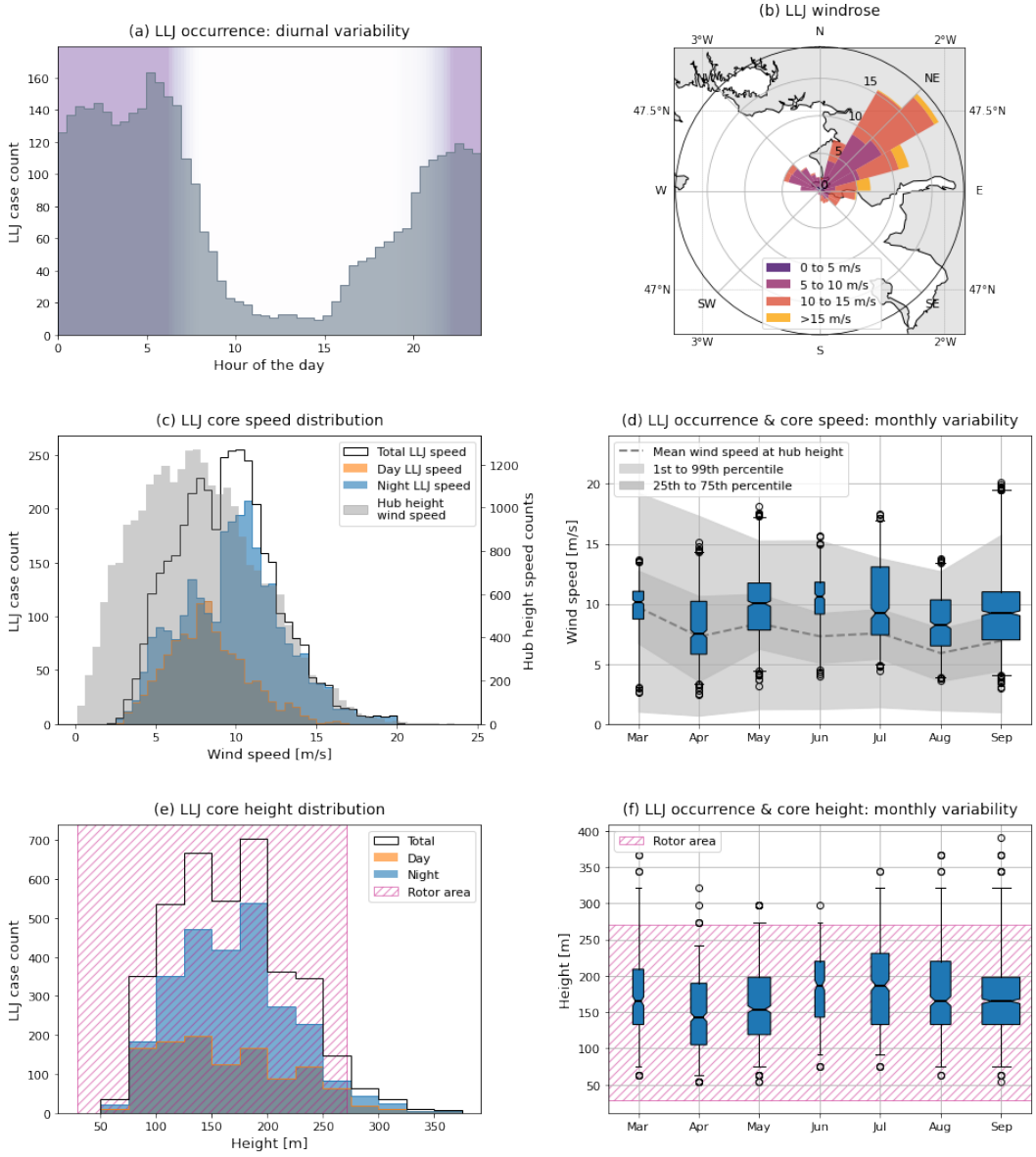

Figure 13. Low-level jet statistics. (a) Occurrence of LLJ events by time of day, with the purple background denoting nighttime (averaged). (b) Wind rose of LLJ events. (c) Histogram of wind speed at the core of all detected LLJs (black contour), at night (blue), during the day (orange) compared to the histogram of wind speed at the hub height (gray). (d) Statistical monthly variability of LLJ core speed. (e) Distribution of LLJ core heights over the entire period (black contour) at night (blue) and during the day (orange). (f) Statistical monthly variability of LLJ core height.

indicated by a gray dashed line for comparison and its spread is indicated by the two gray areas according to the percentiles,

as explained in the legend. Once again, LLJ core speeds are, on average, higher than hub height speeds yet roughly follow the same monthly trend.

Similarly to Fig. 13c and d, Fig. 13e and f present statistics on the height of the LLJ detected. The histograms of LLJ core height for *daytime* and *nighttime* in Fig. 13e, do not show any significant differences in shape. LLJ core heights range from 50 to 350 m above sea level, although most observations lie between 100 and 250 m. The hatched area in both figures corresponds to the wind turbine rotor and moreover indicates that most LLJ cores reach the upper half of the rotor area. The monthly evolution in LLJ height (Fig. 13f) does not exhibit any pronounced trend but nonetheless confirms once again that in most instances time low-level jet cores lie well inside the rotor area. A slight increase in both core speed and core height is nevertheless observed in June, which is also the month with the lowest number of LLJ cases. In April and May, LLJ cores are observed at slightly lower altitudes than in the other months of the dataset, but not to a very significant extend. However, these observations are to be analysed with care as the spread of values for each month revealed by the boxplots is rather high.

3.5 LLJ and high wind shear: cross-referenced statistics

Given that an LLJ is by definition a low-altitude maximum in a wind profile, its presence often implies high wind shear values from the core down to the ground or sea. The shear caused by LLJs is not alawys high, though the link between these two phenomena can be explored by relating the number of LLJ observations to the shear values. In Fig. 14, histograms of the shear exponent for all valid profiles (black) and profiles with and without LLJs (orange and blue, respectively) clearly indicate that LLJs are associated with higher shear. Calculations show an average shear value of 0.21 for LLJ-featuring profiles, versus 0.11 for all profiles and 0.09 for non-LLJ profiles only. In the studied dataset, profiles with $\alpha > 0.2$ account for 30.3% of all the time share. In the non-LLJ subset, this ratio drops to 25.7%, while in the LLJ-subset it rises to 56.2%.

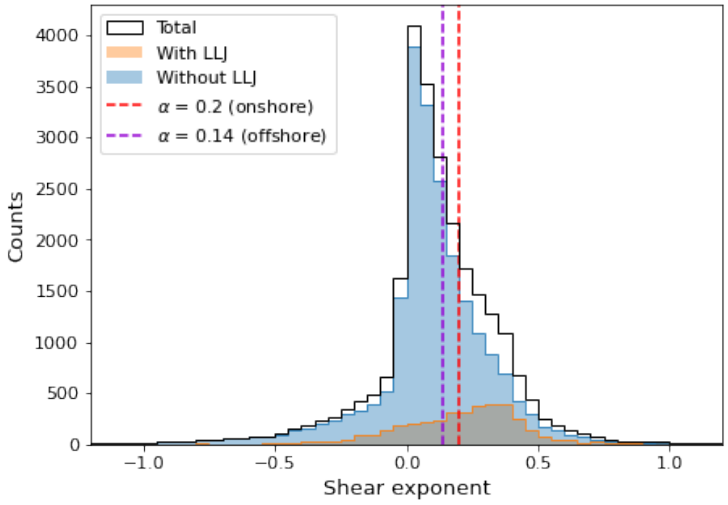

Figure 14. Wind shear histograms for LLJ and non-LLJ subsets

3.6 Application to the production of 10 MW, 15 MW, and 22 MW wind turbines

	10 MW	15 MW	22 MW
Rotor diameter [m]	198	241	283
Hub height [m]	119	150	170
Cut-in speed [m/s]	4	3	3
Cut-out speed [m/s]	25	25	25
Rated speed [m/s]	11.0	10.65	10.94
Operating rate	84.5%	84.5%	84.6%
Capacity factor	52%	51.9%	49.5%
Mean power [MW]	5.2	7.8	10.9
Mean wind speed at the hub [m/s]	7.43	7.68	7.78
REWS [m/s]	7.44	7.70	7.80

Table 4. Characteristics of the turbines studied and key production results.

This section analyses the potential power production based on the 10-min data at the site for three large-scale wind turbines: *IEA 10MW 198 RW* [3], *IEA 15* MW *240 RWT* [4], and *IEA 22 280 RWT* [5].

Power is computed for each turbine using the rotor equivalent wind speed (REWS) method proposed by Wagner et al. (2009) and adapted by Murphy et al. (2020) to account for shear across the rotor. The method used herein employs all measurement heights available within the rotor area of each turbine. This simple approach does not take into account all the complexity of wind energy harvesting (e.g. turbulence intensity, maintenance) but does provide perspective for the observations conducted. Note that the dataset does not cover the whole year and moreover some months are underrepresented, thereby limiting the generalization of a month-to-month statistical analysis.

The analysis of global power production metrics, as summarized in Table 4, shows that over the studied period, the operating rate of all studied turbines is high (>84%) with a slight advantage for the 22 MW turbine. The observed capacity factor slightly decreases with turbine rated power: 52%, 51.9%, 49.5% for 10 MW, 15 MW, and 22 MW, respectively. This result is high compared with capacity factors typically encountered offshore Costanzo et al. (2023). The average 10-min power production equals 5.2 MW, 7.8 MW, and 10.9 MW; these remarkable performances could be obtained, at least partly, thanks to a rated power reached at 11 $\mathrm{m/s}$ for the chosen reference turbines.

Over the studied period, which mainly consists of spring and summer 2020, daytime and nighttime represent 59% and 41% of the total time, respectively. However, considering that the production rate is higher at night than during the day (see Fig. 15b), overall production is distributed differently: 51% of the total electricity is produced during the day and 49% at night. Over a

[3]https://github.com/IEAWindTask37/IEA-10.0-198-RWT, last access: 10 June 2024
[4]https://github.com/IEAWindTask37/IEA-15-240-RWT, last access: 10 June 2024
[5]https://github.com/IEAWindTask37/IEA-22-280-RWT, last access: 10 June 2024

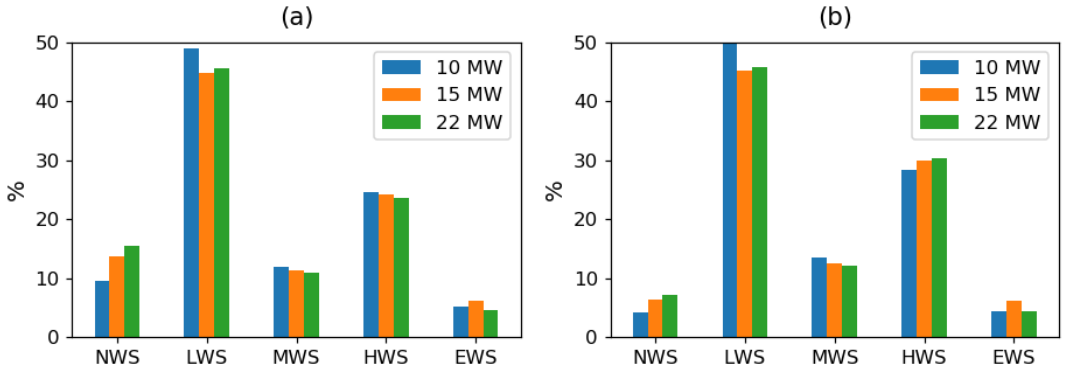

Figure 15. Participation of each shear exponent range to (a) total production time and (b) total production (amount of electricity produced).

full year, it is likely that the nighttime will contribute more to total electricity production (in considering the longer nights during autumn and winter). Additionally, stronger winds are expected during wintertime at Le Croisic.

Low-level jets are observed in 15.5% of all profiles and 17.6% of cases when electricity production is possible. However, for these three turbines, the mean production during LLJs (Fig. 16b) is slightly lower than the overall mean production. Having a production share that exceeds the share of time spent producing at a lower mean power rate might appear counterintuitive. One explanation for this finding is that within the LLJ subset the production rate is over 93%, as compared to the non-LLJ subset (with a production rate of 83%). This higher rate makes LLJs globally profitable in terms of energy production and moreover compensates for a mean production slightly below average.

Mean production time (i.e. time when the wind is between cut-in and cut-out speed) and total production (in terms of produced energy) are given in Fig. 15a and b for the 5 shear conditions set forth in Table 3. For all turbines tested, the addition of LWS and MWS events (as defined in the IEC recommendations of IEC (2009)) represent most of the production time (around 60%) and most of the total production during the period (60%). Higher shear events (including HWS and EWS) account for nearly 30% of the time and almost 35% of total production. NWS represents 8% to 15% of the total production time and 4% to 6% of total electricity production. As the wind turbines increase in diameter, more time is spent in NWS and slightly more energy is produced. This outcome can be correlated with a higher hub height which in turn is associated with a higher REWS. Also suggested here is that NWS events mostly appear during low wind speed events. The mean energy production during NWS events (Fig. 16b), i.e. over 55% less than the overall mean production, confirms this hypothesis. These results are not very sensitive to the wind turbine choice, but larger turbines do tend to produce more at high and negative wind shear.

The cumulative sum of the production times, sorted in descending order, in Fig. 16a, shows that the 26% best production times account for half the total power production, while the 50% best production times represent 80% of total production. These results underscore the fact that most energy is produced during a small number of high production periods; they are not significantly affected by the choice of turbine type.

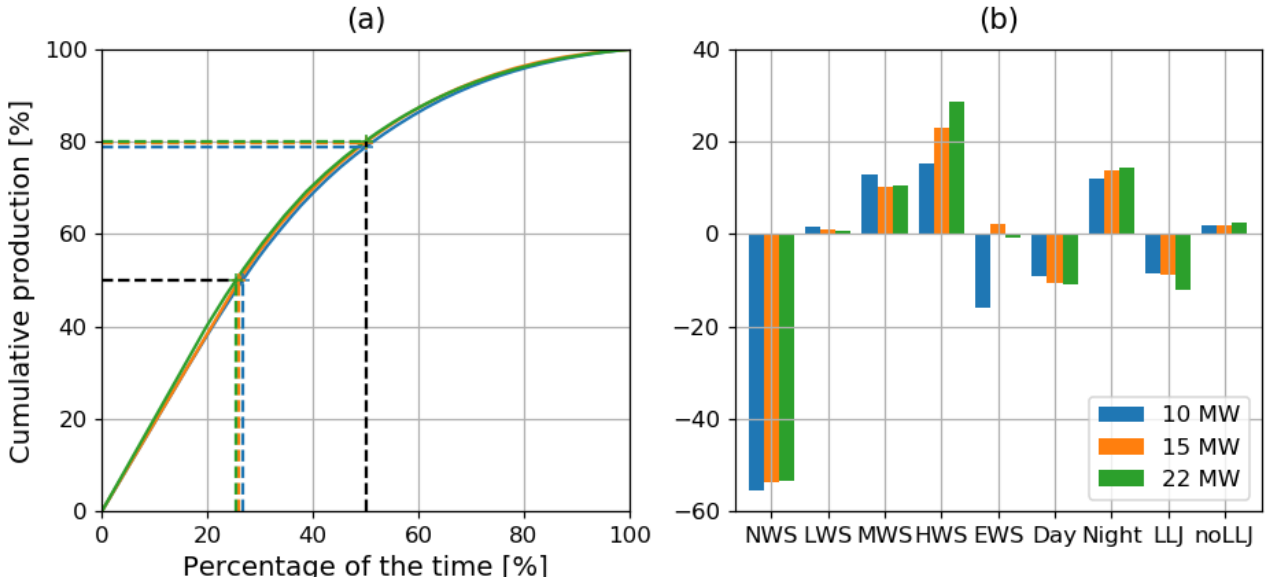

Figure 16. (a) Cumulative sum of 10-min production periods sorted in descending order and (b) percentage of difference between mean 10-min production in each shear category and overall mean 10-min production for the three turbines considered: 10 MW (blue), 15 MW (orange), and 22 MW (green).

Figure 16b illustrates the ratio between the mean power production of each type of event relative to the overall mean 10-min production. It is clear once again that the shear exponent strongly influences the power production, along with the day/night distribution, but LLJs constitute a less significant factor. These results are only slightly affected by the choice of turbine, except for HWS and EWS, whereby larger rotors tend to perform better than for smaller turbines.

4 Discussion

The methodology described in Sec.2 shows how both time and space information compiled from a limited number of PPI scans can be used to increas vertical resolution. This approach relies mainly on horizontal homogeneity within the volume used for wind profile reconstruction, i.e. more than a $1\ \mathrm{km}$ extension in the present case. The validation process for the homogeneity hypothesis is twofold: within each scan, as evaluated by the quality index; and between two horizontally-spaced measurements, as evaluated by the correlation coefficient R^2.

The analysis herein reveals that wind speed reconstruction is more accurate for *sea wind*, thus indicating greater homogeneity compared to *land wind*. However, the scan orientation relative to wind direction (along or across LOS) is found to have an equal or sometimes stronger effect on accuracy, suggesting that horizontal homogeneity within each scan is not a major concern in the tested configuration. This result may be invalid if a smaller azimuth range is used for *HWS* reconstruction.

Concerning the homogeneity between horizontally-spaced measurements, the correlation is clearly affected by wind direction, with R^2 being lower under *sea wind* conditions than *land wind* conditions. The scan orientation relative to wind direction would seem to play a secondary role in this case. The correlation also clearly increases with increasing altitude.

This result is likely to be valid above a smooth surface such as the sea, but care should be taken closer to the shore or in the presence of obstacles such as islands. In the absence of local reference measurements, the homogeneity study is based on relative fitting indicators that do not provide absolute error quantification. However, the observed multiple correlations are considered to be strong enough evidence for validity of the proposed approach.

The 10-min statistical convergence analysis (Sec. 2.2.3) assumes that the integral turbulent scale is proportional to height, which is a commonly adapted approach for wind speed measurements, including those with ultrasonic anemometers. The turbulent scale is also assumed to be uniform regardless of the sLiDAR direction with respect to the wind direction. In reality, such is not the case in the atmosphere as turbulent structures are elongated in the streamwise direction. The approach implemented for the analysis is therefore expected to be conservative.

In Fig. 11b, where wind shear exponents are sorted into *land wind* and *sea wind* categories, the *sea wind* distribution largely resembles the *daytime* distribution while the *land wind* distribution is very similar to the *nighttime* distribution. However, a day/night filtering does not directly correspond to a directional prevalence. Even though a systematic link between the pairs cannot be established based solely on the similarity of histograms, a connection can still be made. On the one hand, *nighttime* over land is often associated with a stable thermal stratification that leads to a higher shear exponent compared to the unstable conditions often observed during *daytime* and associated with lower shear exponents. On the other hand, *sea wind*, due to lower surface roughness, is associated with a lower power exponent compared to *land wind*. Therefore, both sea wind and daytime are associated with a low shear, while both nighttime and land wind are associated with a high shear, as an explanation of the similarities observed. Further similar observations of the influence of thermal stability and surface roughness on the wind shear have been reported in Hanafusa et al. (1986) and Irwin (1979).

Low-level jets (LLJs) observed near the coast and described in Sec.3.4 can be caused by multiple physical processes. At the studied site, LLJs were mostly observed to come from land (northeastern direction) and at night, with a monthly observation rate within the range of 8-30%. Even though the deployed measurement set-up allows for measurements as high as 500 m above sea level, LLJ cores were primarily observed between 100 and 250 m. These observations do not fit the description of coastal LLJs provided by Parish (2000); Nunalee and Basu (2014) or by Rijo et al. (2018): these authors observed, at several places around the world, synoptic-driven coastal jets blowing parallel to the coast and intensified by mesoscale forcing, especially by a cross-coast barocline due to temperature gradients and/or a topography change at the sea/land transition. In their studies, the core height range of these coastal LLJs was on the order of the marine boundary-layer (300-500 m), which is considerably greater than that in the present study. The observed LLJs are therefore likely to be caused by other processes. Svensson et al. (2019) observed LLJs near the coast of the Baltic Sea blowing normal to the coastline. They suggested that these nighttime LLJs may be formed by warm air advection over the sea or by the advection of nighttime land-generated LLJs across the coastline into the sea. The latter possibility seems to agree well with the observations, whereby nocturnal LLJs, typically observed over land at night (see for example Mitchell et al. (1995)), would persist for a number of kilometers offshore. Similar observations

have been reported by (Kalverla et al., 2019). In addition, when wind blows from the land, the coastline becomes the site of a rough-to-smooth surface transition that is likely to favor an acceleration of the wind close to the surface. At night, the streamwise surface temperature gradient imposed by the coastline may also play a role. The data available during the present test campaign are too limited to either achieve full clarity regarding the origins of the observed LLJs or to explain the condition of persistence of land-generated LLJs further offshore. In particular, no evaluation of the thermal stability of the air mass was performed, since it is expected that classical evaluation, from covariance or Richardson bulk, will yield erroneous results in a transitional zone.

5 Conclusions

This paper has presented an original method for measuring a well-resolved vertical profile of horizontal wind speed above the sea in a coastal area. Using a scanning Doppler wind LiDAR configured to produce PPI scans from the shore at just 6 elevation angles above the sea surface, the vertical wind profile can be probed from 20 m to 450 m above sea level with 27 intermediate altitudes, in relying on a horizontal homogeneity hypothesis within a prescribed horizontal range. Homogeneity has been evaluated in this study within each scan and between horizontally spaced reconstruction measurements. Despite the presence of the coast, the homogeneity hypothesis could be successfully validated, although slightly more uncertainty was observed close to the sea surface in the case of wind coming from the land. The described configuration makes it possible to reach altitudes not available with conventional profilers, which may be valuable both for the design of increasingly tall offshore wind turbines and for a better understanding and parameterization of the ABL at high altitude, especially in the coastal zone.

By taking into account the spatial resolution of each single PPI scan, the statistical error associated with the convergence of the 10-min horizontal wind speed estimation from the proposed method is determined to be of the same order of magnitude as that of an ultrasonic anemometer or a wind vane placed under the same conditions. The error shows a dependence on the angle between wind direction and sLiDAR line of sight; it is found to be slightly lower than that of an ultrasonic anemometer for wind speeds below 10 $\mathrm{m/s}$ and slightly higher for wind speeds above, thus indicating good reliability of the approach being implemented.

The AROME reanalysis database has been used to evaluate the coherence of these results at multiple levels. The comparison tools include wind speed distributions, wind roses at several heights and monthly means of the vertical profiles. In considering the uncertainties involved, good agreement has been reached between the sLiDAR results and the reanalysis data, hence validating the method and its set-up within the tested configuration. Further work will consist of testing the methodology under different conditions versus reference measurements (e.g. other LiDAR set-ups, metmasts) in order to better document the conditions of validity and method limitations. A possible further improvement would be to evaluate the method's ability to estimate the turbulence level.

Using a sLiDAR mounted at the shore has the advantage of eliminating the need for stabilization and/or compensation for wave-induced motion, which is a non-trivial problem for a floating LiDAR. However, the range of the device, here 3 km, and the homogeneity requirements do limit the distance from the shore where the wind profile can be reconstructed, therefore

restricting the application to offshore situations. A longer-range scanning wind LiDAR installed at the shore or on a fixed platform might be needed to measure vertical wind profiles further from the shore.

After validation, the proposed method was applied to a 7-month test campaign conducted on France's Atlantic coast in March-September 2020, generating a unique dataset for use in assessing the wind resource and documentating of the presence of LLJs and high wind shear events heretofore never reported along the northeastern Atlantic coast. In the observation data, periods with a shear exponent greater than the IEC reference values for onshore and offshore wind turbines were observed more than 30% of the time, which would correspond to 33% of the total energy production of a 15 MW wind turbine placed at the observation site. This analysis was conducted on the potential production of 10 MW, 15 MW, and 22 MW wind turbines; the differences were found to be limited from one turbine type to another. During high wind shear periods, the wind turbine might be subjected to loads above its design load, potentially leading to fatigue and other structural damage.

During the test campaign, low-level jets were observed in about 15% of all 10-minute averaged profiles, in contributing 17% of the production of a 15 MW wind turbine installed at the site. Even if the LLJs are not part of the strongest recorded production events, it is to be noted that during the studied period, energy was produced 93% of the time when LLJs were observed, which is higher than the average production time without LLJs (below 80%). Another observation is that LLJs are often associated with high and extreme wind shear, when considering that in 56.2% of LLJ observations the across-the-rotor shear exponent was greater than $\alpha = 0.2$, versus 25.7% of the time when considering only non-LLJ cases and 30.3% if all cases are taken into account.

The presence of LLJs within the rotor area of a multi-megawatt wind turbine (mainly in the range 150-250 m above mean sea level) entails major consequences for the wind energy industry. Such installations they may be beneficial for total production mainly as a result of their regularity and above average wind speeds, yet they are also associated with shear exponents above the reference design values. These observations are of significant importance in understanding the coastal wind resource, especially since the presence of LLJs is often underestimated by mesoscale models (Nunalee and Basu, 2014).

During the test campaign, LLJs were mostly observed when the wind was coming from the land (northeast wind) as well as at night, thereby suggesting that they are generated inland, cross the coastline and persist in reaching the observation site located 1.5 km offshore. The origin of the observed LLJs remains uncertain, as the discrete profiles provided by the sLiDAR are insufficient to fully verify any hypothesis. This work leads to questionning the dynamic evolution of land-generated nocturnal LLJs that cross the coastline and extend further offshore; also yet to be revealed is the role played by the strong roughness and thermal land-sea transition. The need exists for further investigation into the land-sea micro-meteorology, which impacts both the wind shear and wind veer (beyond the scope of this study) tens of kilometers offshore, where wind farms operate. This work is expected to help pave the way to a clearer understanding of the variability of the offshore wind resource close to the coast, where the dynamics of complex processes remain largely understudied.

Data availability. The raw data used herein can be made accessible upon request.

Author contributions. B.C. conceived, designed and performed the measurement campaign, A.V. proposed and implemented the data treatment methodology, A.V and B.C. performed the data analysis, A.V. drafted the basic version of the paper (as her Master's thesis), A.V. and B.C. were responsible for writing, reviewing and editing, B.C. supervised the project and was the recipient of the funding. All authors have read and agreed to the published version of this manuscript.

Competing interests. Author declare that no competing interest is present.

Acknowledgements. The SEM-REV test site (Centrale Nantes) is gratefully acknowledged for hosting the field experimental campaign and for its technical support. The scanning LiDAR installation was made possible thanks to the framework of the WEAMEC, West Atlantic Marine Energy Community, with funding provided by the Pays de la Loire Region and Europe (European Regional Development Fund) under the WAKEFUL project. This work also contributed to the MATRAC research effort sponsored by ANR-ASTRID under contract no. ANR-18-ASTR-0002.

References

Aird, J. A., Barthelmie, R. J., Shepherd, T. J., and Pryor, S. C.: Occurrence of low-level jets over the eastern US coastal zone at heights relevant to wind energy, Energies, 15, 445, 2022.

Archer, C. L., Colle, B. A., Delle Monache, L., Dvorak, M. J., Lundquist, J., Bailey, B. H., Beaucage, P., Churchfield, M. J., Fitch, A. C., Kosovic, B., et al.: Meteorology for coastal/offshore wind energy in the United States: Recommendations and research needs for the next 10 years, Bulletin of the American Meteorological Society, 95, 515–519, 2014.

Cameron, L., Clerc, A., Feeney, S., and Stuart, P.: Remote Wind Measurements Offshore Using Scanning LiDAR Systems, OWA Report, pp. 1–36, 2014.

Cheynet, E., Flügge, M., Reuder, J., Jakobsen, J. B., Heggelund, Y., Svardal, B., Saavedra Garfias, P., Obhrai, C., Daniotti, N., Berge, J., et al.: The COTUR project: remote sensing of offshore turbulence for wind energy application, Atmospheric Measurement Techniques, 14, 6137–6157, 2021.

Costanzo, G., Brindley, G., and Cole, P.: Wind energy in Europe - 2022 statistics and the outlook for 2023-2027, 2023.

Debnath, M., Doubrawa, P., Optis, M., Hawbecker, P., and Bodini, N.: Extreme wind shear events in US offshore wind energy areas and the role of induced stratification, Wind Energy Science, 6, 1043–1059, 2021.

Díaz, H. and Soares, C. G.: Review of the current status, technology and future trends of offshore wind farms, Ocean Engineering, 209, 107 381, 2020.

Djath, B., Schulz-Stellenfleth, J., and Cañadillas, B.: Study of Coastal Effects Relevant for Offshore Wind Energy Using Spaceborne Synthetic Aperture Radar (SAR), Remote Sensing, 14, 1688, 2022.

Emeis, S.: Wind speed and shear associated with low-level jets over Northern Germany, Meteorol. Z, 23, 295, 2014.

Garratt, J. R.: The atmospheric boundary layer, Earth-Science Reviews, 37, 89–134, 1994.

George, W. K., Beuther, P. D., and Lumley, J. L.: Processing of random signals, in: Proceedings of the Dynamic Flow Conference 1978 on Dynamic Measurements in Unsteady Flows, pp. 757–800, Springer, 1978.

Gryning, S.-E. and Floors, R.: Carrier-to-noise-threshold filtering on off-shore wind lidar measurements, Sensors, 19, 592, 2019.

Hanafusa, T., Lee, C. B., and Lo, A. K.: Dependence of the exponent in power law wind profiles on stability and height interval, Atmospheric Environment (1967), 20, 2059–2066, 1986.

Hasager, C. B., Peña, A., Christiansen, M. B., Astrup, P., Nielsen, M., Monaldo, F., Thompson, D., and Nielsen, P.: Remote sensing observation used in offshore wind energy, IEEE Journal of Selected Topics in Applied Earth Observations and Remote Sensing, 1, 67–79, 2008.

IEC: Wind turbines—design requirements, 2005.

IEC: Wind turbines—design requirements for offshore wind turbines, 2009.

Irwin, J. S.: A theoretical variation of the wind profile power-law exponent as a function of surface roughness and stability, Atmospheric Environment (1967), 13, 191–194, 1979.

Justus, C. G., Hargraves, W. R., Mikhail, A., and Graber, D.: Methods for Estimating Wind Speed Frequency Distributions, Journal of Applied Meteorology (1962-1982), 17, 350–353, http://www.jstor.org/stable/26178009, 1978.

Kaimal, J. C. and Finnigan, J. J.: Atmospheric boundary layer flows: their structure and measurement, Oxford university press, 1994.

Kalverla, P. C., Duncan Jr., J. B., Steeneveld, G.-J., and Holtslag, A. A. M.: Low-level jets over the North Sea based on ERA5 and observations: together they do better, Wind Energy Science, 4, 193–209, https://doi.org/10.5194/wes-4-193-2019, 2019.

Mahrt, L.: Stratified atmospheric boundary layers, Boundary-Layer Meteorology, 90, 375–396, 1999.

Mahrt, L., Vickers, D., and Andreas, E. L.: Low-level wind maxima and structure of the stably stratified boundary layer in the coastal zone, Journal of Applied Meteorology and Climatology, 53, 363–376, 2014.

Martinez, A. and Iglesias, G.: Mapping of the levelised cost of energy for floating offshore wind in the European Atlantic, Renewable and Sustainable Energy Reviews, 154, 111 889, 2022.

Mitchell, M. J., Arritt, R. W., and Labas, K.: A climatology of the warm season Great Plains low-level jet using wind profiler observations, Weather and Forecasting, 10, 576–591, 1995.

Murphy, P., Lundquist, J. K., and Fleming, P.: How wind speed shear and directional veer affect the power production of a megawatt-scale operational wind turbine, Wind Energy Science, 5, 1169–1190, https://doi.org/10.5194/wes-5-1169-2020, 2020.

Nunalee, C. G. and Basu, S.: Mesoscale modeling of coastal low-level jets: implications for offshore wind resource estimation, Wind Energy, 17, 1199–1216, 2014.

Parish, T. R.: Forcing of the summertime low-level jet along the California coast, Journal of Applied Meteorology and Climatology, 39, 2421–2433, 2000.

Paskin, L., Conan, B., Perignon, Y., and Aubrun, S.: Evidence of Ocean Waves Signature in the Space–Time Turbulent Spectra of the Lower Marine Atmosphere Measured by a Scanning LiDAR, Remote Sensing, 14, 3007, 2022.

Pichugina, Y., Brewer, W., Banta, R., Choukulkar, A., Clack, C., Marquis, M., McCarty, B., Weickmann, A., Sandberg, S., Marchbanks, R., et al.: Properties of the offshore low level jet and rotor layer wind shear as measured by scanning Doppler Lidar, Wind Energy, 20, 987–1002, 2017.

Pichugina, Y. L., Banta, R. M., Brewer, W. A., Sandberg, S. P., and Hardesty, R. M.: Doppler lidar–based wind-profile measurement system for offshore wind-energy and other marine boundary layer applications, Journal of Applied Meteorology and Climatology, 51, 327–349, 2012.

Ramirez, L.: Offshore wind in Europe, key trends and statistics, 2022.

Rijo, N., Semedo, A., Miranda, P. M., Lima, D., Cardoso, R. M., and Soares, P. M.: Spatial and temporal variability of the Iberian Peninsula coastal low-level jet, International Journal of Climatology, 38, 1605–1622, 2018.

Rogers, D. P.: Coastal meteorology, Reviews of Geophysics, 33, 889–895, 1995.

Rubio, H., Kühn, M., and Gottschall, J.: Evaluation of low-level jets in the southern Baltic Sea: a comparison between ship-based lidar observational data and numerical models, Wind Energy Science, 7, 2433–2455, https://doi.org/10.5194/wes-7-2433-2022, 2022.

Sempreviva, A. M., Barthelmie, R. J., and Pryor, S.: Review of methodologies for offshore wind resource assessment in European seas, Surveys in Geophysics, 29, 471–497, 2008.

Shaw, W. J., Berg, L. K., Debnath, M., Deskos, G., Draxl, C., Ghate, V. P., Hasager, C. B., Kotamarthi, R., Mirocha, J. D., Muradyan, P., et al.: Scientific challenges to characterizing the wind resource in the marine atmospheric boundary layer, Wind Energy Science, 7, 2307–2334, 2022.

Shimada, S., Goit, J. P., Ohsawa, T., Kogaki, T., and Nakamura, S.: Coastal wind measurements using a single scanning LiDAR, Remote Sensing, 12, 1347, 2020.

Shimada, S., Kogaki, T., Konagaya, M., Mito, T., Araki, R., Ueda, Y., and Ohsawa, T.: Validation of near-shore wind measurements using a dual scanning light detection and ranging system, Wind Energy, 2022.

Simon, E.: Determination of an Optimum Sector Size for Plan Position Indicator Measurements using a Long Range Coherent Scanning Atmospheric Doppler LiDAR., 2015.

Smedman, A.-S., Tjernström, M., and Högström, U.: Analysis of the turbulence structure of a marine low-level jet, Boundary-layer meteorology, 66, 105–126, 1993.

Soares, P. M., Cardoso, R. M., Semedo, Á., Chinita, M. J., and Ranjha, R.: Climatology of the Iberia coastal low-level wind jet: weather research forecasting model high-resolution results, Tellus A: Dynamic Meteorology and Oceanography, 66, 22 377, 2014.

Svensson, N., Bergström, H., Rutgersson, A., and Sahlee, E.: Modification of the Baltic Sea wind field by land-sea interaction, Wind Energy, 22, 764–779, 2019.

Veers, P., Dykes, K., Lantz, E., Barth, S., Bottasso, C. L., Carlson, O., Clifton, A., Green, J., Green, P., Holttinen, H., et al.: Grand challenges in the science of wind energy, Science, 366, eaau2027, 2019.

Wagner, D., Steinfeld, G., Witha, B., Wurps, H., and Reuder, J.: Low level jets over the Southern North Sea, Meteorologische Zeitschrift, 28, 389–415, 2019.

Wagner, R., Antoniou, I., Pedersen, S. M., Courtney, M. S., and Jørgensen, H. E.: The influence of the wind speed profile on wind turbine performance measurements, Wind Energy, 12, 348–362, https://doi.org/https://doi.org/10.1002/we.297, 2009.